

Analytic Bijections for Smooth and Interpretable Normalizing Flows

Mathis Gerdès¹ Miranda C. N. Cheng^{1,2,3}

¹Institute of Physics, University of Amsterdam, Netherlands

²Korteweg-de Vries Institute for Mathematics, University of Amsterdam, Netherlands

³Institute for Mathematics, Academia Sinica, Taiwan

{m.gerdes, mcheng}@uva.nl

Abstract

A key challenge in designing normalizing flows is finding expressive scalar bijections that remain invertible with tractable Jacobians. Existing approaches face trade-offs: affine transformations are smooth and analytically invertible but lack expressivity; monotonic splines offer local control but are only piecewise smooth and act on bounded domains; residual flows achieve smoothness but need numerical inversion. We introduce three families of *analytic bijections*—cubic rational, sinh, and cubic polynomial—that are globally smooth (C^∞), defined on all of \mathbb{R} , and analytically invertible in closed form, combining the favorable properties of all prior approaches. These bijections serve as drop-in replacements in coupling flows, matching or exceeding spline performance. Beyond coupling layers, we develop *radial flows*: a novel architecture using direct parametrization that transforms the radial coordinate while preserving angular direction. Radial flows exhibit exceptional training stability, produce geometrically interpretable transformations, and on targets with radial structure can achieve comparable quality to coupling flows with $1000\times$ fewer parameters. We provide comprehensive evaluation on 1D and 2D benchmarks, and demonstrate applicability to higher-dimensional physics problems through experiments on ϕ^4 lattice field theory, where our bijections outperform affine baselines and enable problem-specific designs that address mode collapse.

1 Introduction

Normalizing flows learn probability distributions by transforming a simple base density through invertible maps, enabling exact likelihood computation and efficient sampling. In many cases such as coupling or autoregressive layers, these are built out of basic scalar bijections acting coordinate-wise, making the choice of bijection a key design challenge. This choice fundamentally constrains how expressive a given concrete architecture is, and how stably it can be trained.

Existing scalar bijections face a tradeoff. *Affine transformations* [1] are smooth and analytically invertible, but can only shift and scale. They lack the local expressivity needed to capture multimodal or heavy-tailed structure without many layers. *Monotonic splines* [2] offer fine-grained local control through learnable knots, but are only C^k for finite k (not C^∞) and only actively transform a bounded interval, requiring domain tuning for each application. *Neural autoregressive flows* [3] replace affine transforms with monotonic neural networks, achieving universal approximation but requiring implicit neural network inversion. *Residual flows* [4, 5, 6], Gaussianization flows [7], and related smooth constructions [8] achieve both smoothness and expressivity, but generally re-

quire numerical root-finding for inversion, complicating implementation and adding computational overhead.

We introduce a family of *analytic bijections* that resolve this tradeoff: globally smooth (C^∞), defined on all of \mathbb{R} , analytically invertible in closed form, and supporting both local deformations and global redistribution of probability mass. Our constructions derive from two principles. First, algebraic rational functions whose inverses reduce to solvable cubics, and second, conjugation with monotonic maps like \sinh , yielding three concrete bijection families: *cubic rational*, *sinh*, and *cubic polynomial*. These can serve as drop-in replacements for affine or spline transformers in existing coupling architectures.

Beyond improving coupling flows, we develop a novel architecture that leverages these bijections in a fundamentally different way. *Radial flows* decompose space into radius and angular direction, applying scalar bijections only to the radial coordinate. Unlike coupling flows, whose bijection parameters are generated by neural network conditioners, radial flow parameters are learned directly as model weights. Radial flows exhibit exceptional training stability, produce geometrically interpretable transformations, and, on targets with natural radial structure, achieve comparable quality to coupling flows with orders of magnitude fewer parameters. We further extend radial flows with angular dependence, including a Fourier parametrization in 2D where the learned coefficients directly reveal which angular modes the flow uses to match the target.

Paper organization. Section 2 reviews normalizing flows and existing scalar bijections. Section 3 presents our analytic bijections: construction principles, concrete expressions, and how to include learnable parameters for stable training. Section 4 describes flow architectures leveraging these bijections, with emphasis on radial flows. Section 5 provides comprehensive evaluation: 1D density estimation, coupling layer integration, radial flow benchmarks on 2D targets, and a physics application to lattice field theory. Section 6 concludes with a discussion on future directions and limitations.

1.1 Contributions

Our two primary contributions are: novel scalar bijections and novel flow architectures.

1. **Analytic bijections.** We introduce three families of scalar bijections—*cubic rational*, *sinh*, and *cubic polynomial*—derived from two construction principles: algebraic rational functions and conjugation with nonlinear monotonic maps. Unlike existing alternatives, these bijections automatically and simultaneously satisfy five desiderata: global smoothness (C^∞), unbounded domain, closed-form inverses, tractable Jacobians, and expressive parametrization supporting both local deformations and global effects. Table 1 summarizes how they compare to affine, spline, and residual flows such as mixture CDF transforms [6].
2. **Radial flow architectures.** We develop a novel class of normalizing flows based on radial decomposition: transforming the radius $r = \|\mathbf{x}\|$ while preserving angular direction. These *radial flows* exhibit exceptional training stability (tolerating learning rates an order of magnitude higher than coupling flows) and produce interpretable, geometrically intuitive transformations without requiring dense neural networks. We further extend radial flows with angular dependence, including an explicit Fourier parametrization in 2D where each of the 50–300 learned parameters has direct geometric meaning.
3. **Evaluation.** We validate our methods across multiple settings: (i) 1D density estimation, demonstrating monotonic improvement with bijection depth; (ii) coupling layer integration,

showing competitive or superior performance to spline baselines; (iii) radial flow benchmarks on both unimodal and multimodal 2D targets, highlighting qualitative smoothness advantages and interpretability with directly inspectable parameters rather than opaque neural networks; (iv) application to ϕ^4 lattice field theory on a 20×20 lattice, demonstrating scalability to higher dimensions and physics-motivated problem-specific design.

Our bijections serve as drop-in replacements in existing coupling architectures, while our radial flows offer a complementary paradigm suited to problems where smoothness, interpretability, or simplicity are priorities.

2 Background and Related Work

2.1 Normalizing Flows

Normalizing flows [9, 10, 11] are generative models that learn a probability distribution by defining an invertible transformation $f_\theta : \mathbb{R}^d \rightarrow \mathbb{R}^d$ from a simple base distribution (typically Gaussian) to the target. The model density is given by the change of variables formula:

$$q_\theta(x) = \rho(f_\theta^{-1}(x)) \left| \det \frac{\partial f_\theta^{-1}}{\partial x} \right|, \quad (1)$$

where ρ is the base density. Flows are typically constructed as compositions $f_\theta = f^{(L)} \circ \dots \circ f^{(1)}$ of simpler bijective layers, where each layer $f^{(\ell)}$ has an efficiently computable log-determinant Jacobian.

The key architectural challenge is designing bijective layers that are both expressive and computationally tractable. Three main paradigms have emerged: **Autoregressive flows** [12, 13, 3] transform each dimension sequentially, conditioning on all previous dimensions, yielding a triangular Jacobian. Similarly, **coupling flows** [14, 1, 15] partition dimensions into “active” and “passive” subsets, transforming the active coordinates using parameters generated from the passive ones. **Residual flows** [5, 16] use invertible residual networks with Lipschitz constraints, providing an alternative to the partitioning structure of coupling layers. **Continuous normalizing flows** [17, 18] define the transformation as the solution to an ordinary differential equation, providing maximum flexibility at higher computational cost.

2.2 Coupling Layers and Scalar Bijections

In order to define coupling layers, we first partition the input $x \in \mathbb{R}^d$ into “passive” coordinates $x_{\text{pass}} \in \mathbb{R}^{d_1}$ and “active” coordinates $x_{\text{act}} \in \mathbb{R}^{d_2}$, with $d = d_1 + d_2$. The passive coordinates remain unchanged, while the active coordinates are transformed using parameters generated by a neural network (the *conditioner*) that takes the passive coordinates as input:

$$y_{\text{pass}} = x_{\text{pass}}, \quad y_{\text{act}} = h(x_{\text{act}}; \theta(x_{\text{pass}})), \quad (2)$$

where h is a scalar bijection applied element-wise, and $\theta = g_\phi(x_{\text{pass}})$ are the bijection parameters output by the conditioner network. The Jacobian is triangular, so its log-determinant reduces to a sum over active coordinates: $\log |\det J| = \sum_i \log |h'(x_{\text{act},i})|$.

The choice of scalar bijection h critically affects expressivity, and thus the number of coupling layers required to achieve a given level of expressivity. **Affine coupling** [1] uses $h(x) = e^s x + t$, which is simple and stable but limited to global scaling and shifting. **Monotonic splines** [2, 19]

use piecewise rational-quadratic functions with learnable knots, offering local control over the transformation but are not smooth and only actively transform a bounded interval (extending linearly outside). **Residual flows** [4, 5, 6] and **Smooth Normalizing Flows** [8] are globally smooth but require numerical inversion via root-finding. Recent work on **B-spline flows** [20] achieves C^k smoothness for arbitrary finite k with analytic invertibility for diffeomorphic transformations, though the active transformation is still confined to a bounded interval.

No existing bijection satisfies all desirable properties simultaneously: affine transformations are smooth and analytically invertible but lack local control; splines offer local control and analytic inverses but are only C^1 -smooth and bounded; residual flows are smooth with local control but require numerical inversion. Our analytic bijections (Section 3) aim to combine the favorable properties of all approaches—global smoothness, unbounded domain, closed-form inverses, and local expressivity—as summarized in Table 1.

2.3 Radial Transformations

Radial flows were introduced by Rezende and Mohamed [21] as one of several simple transformations for improving variational inference. Their formulation uses transformations of the form

$$f(x) = x + \beta h(\alpha, r)(x - x_0), \quad \text{where } r = \|x - x_0\|, \quad (3)$$

with $h(\alpha, r) = 1/(\alpha + r)$ and parameters $\alpha > 0$, $\beta \in \mathbb{R}$, and center $x_0 \in \mathbb{R}^d$. This transformation contracts or expands space radially around x_0 , with the effect strongest near the center and decaying as $|x - x_0|^{-1}$. Each such layer has limited expressivity (only two scalar parameters besides the center).

More recently, coordinate-based decompositions have been explored for flows on non-Euclidean manifolds. Rezende et al. [22] developed flows on circles, spheres, and tori by recursively applying 1D circular flows, while Midgley et al. [23] proposed SE(3)-equivariant flows using internal coordinate transformations for molecular systems. These works demonstrate that coordinate decompositions can enable expressive flows respecting geometric structure.

Our radial flow architecture (Section 4.3) builds on this foundation but differs substantially: we use stacked analytic bijections for the radial component, employ multiple learnable centers, and target density estimation with direct parametrization offering exceptional training stability.

3 Analytic Bijections

A key design choice in normalizing flows is the scalar bijection used to transform individual coordinates. We seek bijections that satisfy the following desiderata:

1. **Smoothness:** The map $h : \mathbb{R} \rightarrow \mathbb{R}$ should be smooth (C^∞), ensuring smooth learned densities.
2. **Global domain:** The bijection should be defined on all of \mathbb{R} , not restricted to a bounded interval.
3. **Analytic invertibility:** Both forward and inverse maps should be computable in closed form without numerical root-finding.
4. **Tractable Jacobian:** The derivative $h'(x)$ should be efficiently computable for the log-determinant.

5. **Expressive parametrization:** The bijection should facilitate *local* deformations, transformations whose effect diminishes smoothly with distance, so that $h(x) \rightarrow x$ as $|x| \rightarrow \infty$. Additionally, some bijections may support *global* effects: either a uniform scaling (as in affine transformations), or an asymptotic shift where the slope returns to unity but distant points are displaced by a constant offset.

Table 1 summarizes how existing scalar bijections fall short: affine transforms lack local control, splines sacrifice smoothness and global domain, and mixture CDFs require numerical inversion. Our constructions (Sections 3.2.1–3.2.3) achieve all five properties simultaneously.

Table 1: Comparison of scalar bijection properties. Our analytic bijections satisfy all desiderata.

Method	Smooth	Global	Analytic inverse	Local control
Affine (Real NVP)	✓	✓	✓	✗
Monotonic splines	C^k only	✗ ¹	✓	✓
Residual flows	✓	✓	✗	✓
<i>This work</i>				
Cubic rational	✓	✓	✓	✓
Sinh	✓	✓	✓	✓
Cubic polynomial	✓	✓	✓	✓

We now present two construction principles that yield bijections satisfying all five desiderata.

3.1 Construction Methods

Our two strategies differ in their underlying mathematical structure. The first exploits *algebraic equations*: carefully chosen rational functions whose inverses reduce to solvable polynomial equations. The second uses *conjugation*: wrapping a simple shift $x \mapsto x + \delta$ between a nonlinear map g and its inverse, turning translation into a smooth nonlinear deformation. Both approaches yield globally smooth bijections with closed-form inverses, but differ in their parametrization and the types of transformations they naturally express.

3.1.1 Algebraic rational functions

First, we consider algebraic expressions, where the relationship between input and output variables x and y is specified by some polynomial equation. Since first order polynomials yield affine transforms, and second order would violate monotonicity, we are led to consider cubic or higher order. On the other hand, fourth and higher order polynomials would preclude analytic invertibility, so we must focus on cubic relationships.

We seek a bijection that locally deviates from the identity, returning to $h(x) \rightarrow x$ as $|x| \rightarrow \infty$. A natural ansatz is $h(x) = x + f(x)$ where $f(x)$ is a localized perturbation. For this we require: (i) $f(x) \rightarrow 0$ as $|x| \rightarrow \infty$, (ii) $1 + f'(x) > 0$ everywhere for bijectivity, and (iii) the resulting equation $y = x + f(x)$ must yield a third order polynomial equation.

The rational form

$$h(x) = x + \frac{\lambda x}{1 + x^2/\sigma^2}, \quad \sigma > 0, \quad (4)$$

satisfies these requirements. The denominator ensures $f(x) \rightarrow 0$ as $|x| \rightarrow \infty$, and rearranging terms yields a cubic equation in x that admits an analytic solution via Cardano's formula. The parameter

¹Splines only actively transform a bounded interval.

σ controls the width of the perturbation (the characteristic scale at which the effect decays), while λ controls the magnitude.

For bijectivity, we require $h'(x) > 0$ for all x . The derivative is given by

$$h'(x) = 1 + \frac{\lambda(1 - x^2/\sigma^2)}{(1 + x^2/\sigma^2)^2}. \quad (5)$$

To ensure strict monotonicity ($h'(x) > 0$), we analyze the minima of $h'(x)$. For $\lambda < 0$, the global minimum occurs at $x = 0$, which requires $\lambda > -1$. Conversely, for $\lambda > 0$, the term reaches its minimum at $|x| = \sqrt{3}\sigma$, which requires $\lambda < 8$. Combining these conditions yields:

$$-1 < \lambda < 8, \quad \sigma > 0. \quad (6)$$

The derivation of these bounds from $h'(x) > 0$ can be found in Appendix A.1.

To allow the perturbation center to vary, we introduce an additional location parameter γ :

$$h(x) = x + \frac{\lambda(x - \gamma)}{1 + (x - \gamma)^2/\sigma^2}. \quad (7)$$

Here γ shifts the center of the “bump,” λ controls its magnitude, and σ its characteristic width.

3.1.2 Conjugation with monotonic functions

Our second construction is based on conjugation: given a strictly monotonic function $g : \mathbb{R} \rightarrow \mathbb{R}$ with known inverse, we define

$$h(x) = g^{-1}(g(x) + \delta). \quad (8)$$

This is bijective for any $\delta \in \mathbb{R}$ since g is bijective, and has the simple derivative

$$h'(x) = g'(x)/g'(h(x)). \quad (9)$$

The map shifts points in the “latent space” defined by g , then maps back. For non-linear g , this creates a non-trivial bijection. However, Eq. (8) alone yields $h(x) \rightarrow x$ as $|x| \rightarrow \infty$ only if g is superlinear². Once we have found a suitable base function g , we can introduce additional parameters to modify its behavior. First, we introduce a scale parameter $\sigma > 0$ and a location parameter γ as before:

$$h(x) = g_{\sigma,\gamma}^{-1}(g_{\sigma,\gamma}(x) + \delta), \quad g_{\sigma,\gamma}(x) = g\left(\frac{x - \gamma}{\sigma}\right). \quad (10)$$

To enable global effects in addition to local deformations, we introduce additional scaling parameters:

$$h(x) = g_{\sigma,\gamma}^{-1}(e^\mu(e^\nu g_{\sigma,\gamma}(x) + \delta)). \quad (11)$$

The parameters $\mu, \nu \in \mathbb{R}$ control asymptotic behavior: for $g = \sinh$, as $|x| \rightarrow \infty$, we have $h(x) \approx x + \sigma(\mu + \nu)$ for large positive x and $h(x) \approx x - \sigma(\mu + \nu)$ for large negative x . This creates a *global shift*: unlike purely local deformations where distant points are unchanged, here distant points are displaced by a constant offset, even though the slope returns to one, $h'(x) \rightarrow 1$. This differs from uniform scaling (as in affine transformations) where $h'(x) = \text{const} \neq 1$ everywhere; here, the nonlinear action is confined to a local region but its cumulative effect propagates globally. Note that the parameter μ could be absorbed into ν and δ , however with the above parametrization the inverse and forward maps are symmetric (switch μ and ν , flip sign of δ, μ, ν).

²Taylor expanding g^{-1} around $g(x)$: $h(x) = x + \delta/g'(x) + O(\delta^2)$. When $\delta \neq 0$, this approaches x if and only if $g'(x) \rightarrow \infty$, i.e., g grows faster than linear.

3.2 Three Specific Bijections

We now present three concrete bijections derived from these construction principles. Table 2 summarizes the parameters across all three bijections and their roles.

3.2.1 Cubic rational bijection

Based on the algebraic construction of Section 3.1, the **cubic rational bijection** is:

$$h(x; \gamma, \lambda, \sigma) = x + \frac{\lambda(x - \gamma)}{1 + (x - \gamma)^2/\sigma^2}, \quad (12)$$

with constraints $-1 < \lambda < 8$ and $\sigma > 0$.

Jacobian. The log-Jacobian (log-derivative) is:

$$\log h'(x) = \log \left(1 + \frac{\lambda(1 - (x - \gamma)^2/\sigma^2)}{(1 + (x - \gamma)^2/\sigma^2)^2} \right). \quad (13)$$

Inverse. Given $y = h(x)$, clearing denominators yields a cubic equation in $(x - \gamma)$ solvable via Cardano's formula. The unique (guaranteed by monotonicity) real root corresponds to the inverse.

Properties. The cubic rational bijection is purely algebraic, requiring no transcendental functions. Within the valid parameter range, it provides smooth local deformations but cannot perform global stretching; it always satisfies $h(x) \rightarrow x$ as $|x| \rightarrow \infty$. Furthermore, the inverse bijection is fundamentally different from the forward one, in contrast to the conjugation-based bijections where inverse and forward transformations are related by simple parameter mappings, and one may thus consider adding both versions to the forward pass of a flow model.

3.2.2 Sinh bijection

Using the conjugation construction with $g(x) = \sinh(x)$, the **sinh bijection** is:

$$h(x; \gamma, \sigma, \delta, \mu, \nu) = \sigma \cdot \operatorname{arcsinh} \left(e^\mu \left(e^\nu \sinh \left(\frac{x - \gamma}{\sigma} \right) + \delta \right) \right) + \gamma, \quad (14)$$

with $\sigma > 0$ and no constraints on $\delta, \mu, \nu \in \mathbb{R}$.

Inverse. By the conjugation structure, the inverse has the same form with sign flips:

$$h^{-1}(y) = \sigma \cdot \operatorname{arcsinh} \left(e^{-\nu} \left(e^{-\mu} \sinh \left(\frac{y - \gamma}{\sigma} \right) - \delta \right) \right) + \gamma. \quad (15)$$

Jacobian. The log-Jacobian can be computed as:

$$\log h'(x) = \mu + \nu + \log \cosh \left(\frac{x - \gamma}{\sigma} \right) - \frac{1}{2} \log (1 + \xi^2), \quad (16)$$

where $\xi = e^\mu (e^\nu \sinh((x - \gamma)/\sigma) + \delta)$. Numerically stable implementations may require handling large arguments asymptotically.

Properties. The sinh bijection supports both local deformations (via δ) and global shift (via μ, ν). For large $|x|$, the asymptotic behavior is $h(x) \approx x \pm \sigma(\mu + \nu)$ as $x \rightarrow \pm\infty$, displacing distant points by a constant offset while the slope returns to unity.

3.2.3 Cubic polynomial bijection

By conjugating the monotonic cubic $g_{a,b}(x) = ax + bx^3$ (where $a, b > 0$) with a translation, we obtain the cubic bijection:

$$h(x; \gamma, \delta, a, b) = g_{a,b}^{-1}(g_{a,b}(x - \gamma) + \delta) + \gamma, \quad (17)$$

where $\delta \in \mathbb{R}$.

Inverse. Both forward and inverse require solving a cubic equation via Cardano’s formula. The inverse is obtained by negating δ :

$$h^{-1}(y) = g_{a,b}^{-1}(g_{a,b}(y - \gamma) - \delta) + \gamma. \quad (18)$$

Jacobian. The log-Jacobian is computed via autodifferentiation in practice, as the explicit formula involves the derivative of the cubic inverse.

Properties. Like the cubic rational bijection, this is purely algebraic and produces only local deformations: since $g(x) = ax + bx^3$ is superlinear, we have $h(x) \rightarrow x$ as $|x| \rightarrow \infty$. It follows the conjugation construction of Section 3.1.2, but differs from the sinh bijection in that it lacks the μ, ν parameters for global shift, and has no explicit scale parameter σ . Instead, the effective scale of the “active” region of the transformation is implicitly determined by the ratio $\sqrt{a/b}$, which sets the characteristic magnitude where cubic and linear terms balance. The parameters a and b thus jointly control both the shape and scale of the latent space, while δ controls the magnitude of the (purely local) deformation via a shift in latent space.

Table 2: Parameter notation across bijection types. All bijections share location γ which controls the location where the transformation deviates non-linearly from the identity.

Symbol	Role	Constraints	Used in
γ	Location (center)	—	All
σ	Scale (width)	$\sigma > 0$	Rational, Sinh
λ	Magnitude	$-1 < \lambda < 8$	Rational
δ	Latent shift	—	Sinh, Cubic
μ, ν	Global shift	—	Sinh
a, b	Polynomial coefficients	$a, b > 0$	Cubic

3.3 Parametrization and Stability

The expressivity of our bijections is a double-edged sword: parameter values near the constraint boundaries can produce extreme transformations with very large or small Jacobians. Careful reparametrization is essential for stable training and to enforce valid parameter ranges.

3.3.1 Enforcing constraints

Network outputs are unconstrained real numbers. We map these “raw” parameters $\theta \in \mathbb{R}$ to valid bijection parameters via differentiable transforms:

- **Positivity** ($\sigma, a, b > 0$): Use $\text{softplus}(\theta) = \log(1 + e^\theta)$ plus a small $\epsilon > 0$.
- **Bounded intervals** ($-1 < \lambda < 8$): Use sigmoid with appropriate affine rescaling.
- **Compressed range** (μ, ν): Use $\text{arcsinh}(\theta)$ to allow large values while dampening growth.

3.3.2 Stability in different contexts

We find that different contexts require different parametrization strategies:

1D flows. For stacks of scalar bijections, parameters are learned directly as described above. Initialization near neutral values (e.g., $\lambda \approx 0, \delta \approx 0$) ensures the initial flow is close to identity.

Coupling layers. In coupling layers, where a neural network generates the bijection parameters, controlling the initialization scale of the conditioner’s final layer is critical. Standard initialization often yields parameter values that drive the bijection toward extreme transformations early in training. We mitigate this by initializing the flow close to the identity by scaling down the final layer weights or biases that feed into parameter transforms, and by compressing the parameter transforms, for instance using $\mu = \text{arcsinh}(\theta/10)$ instead of $\mu = \text{arcsinh}(\theta)$. See Appendix A.4 for parametrization details.

3.4 Properties and Comparison

Having introduced our three bijection families, we now discuss practical considerations for their use.

Illustrative comparison. Figure 1 visualizes three distinct types of transformation behavior:

- **Local deformation** (cubic rational): The bijection deviates from identity in a localized region but $h(x) \rightarrow x$ as $|x| \rightarrow \infty$. Any region of high slope (compression) is compensated by a region of low slope (expansion), so probability mass is redistributed locally.
- **Global shift** (sinh with $\mu, \nu \neq 0$): The slope returns to unity for large $|x|$, but distant points are displaced by a constant offset $\pm\sigma(\mu + \nu)$. Local nonlinear action propagates globally, shifting probability mass without uniform scaling.
- **Uniform scaling** (affine): The slope $h'(x) = e^s$ is constant everywhere, uniformly compressing or expanding the entire distribution.

Our analytic bijections span the first two behaviors; uniform scaling is achieved by standard affine layers. When composed, these behaviors combine: a flow can perform local corrections, global shifts, and uniform scaling as needed.

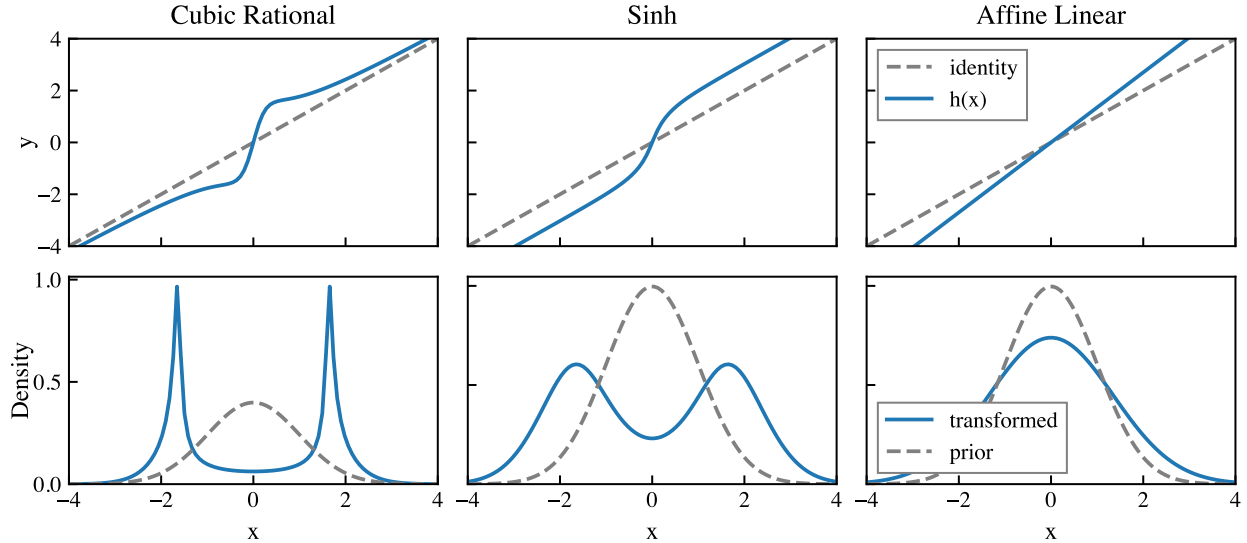


Figure 1: Three types of bijection behavior. **Top row:** Bijection functions $h(x)$ (solid) vs. identity (dashed). **Bottom row:** Resulting density (solid) when transforming a standard normal prior (dashed). *Left* (cubic rational): Local deformation creates bimodal structure while $h(x) \rightarrow x$ for large $|x|$. Thus, “stretching” in some parts is compensated by “compressing” in a nearby region. *Middle* (sinh): Local “stretching” displaces distant points by a constant offset. *Right* (affine): Uniform scaling compresses or expands the distribution while preserving its overall shape.

Computational cost. The cubic rational and cubic polynomial bijections require evaluating Cardano’s formula, involving cube roots and a few arithmetic operations. The sinh bijection uses transcendental functions (\sinh , arcsinh , \exp , \log) which are slightly more expensive but highly optimized in modern numerical libraries. In practice, the bijection cost is negligible compared to neural network evaluations in coupling layers.

Expressivity–stability tradeoff. Unlike affine transforms which have no “dangerous” parameter regions at finite values, our bijections can achieve arbitrarily steep transformations. This expressivity comes at the cost of requiring careful parametrization (Section 3.3); similar considerations arise in the theoretical analysis of depth and conditioning in flows [24]. Splines face a similar tradeoff with respect to knot placement and slope bounds, which are thus usually restricted.

4 Flow Architectures

Having established our analytic bijections in Section 3, we now present flow architectures that leverage them. We begin by demonstrating their applicability to existing paradigms to validate our bijections work as drop-in replacements for existing architectures: one-dimensional stacking (Section 4.1) and coupling layers (Section 4.2). We then introduce a novel class of radial flow architectures (Section 4.3), which decompose transformations in polar coordinates and offer distinct advantages in training stability and interpretability. Finally, we present extensions incorporating angular dependence (Section 4.4) and a highly interpretable 2D variant using Fourier expansions (Section 4.5).

4.1 One-Dimensional Flows

The simplest architecture is direct composition: given K scalar bijections h_1, \dots, h_K , each of which may be of different type, the flow is $f = h_K \circ \dots \circ h_1$. Each bijection generally uses different parameters, and the log-Jacobian is simply the sum of individual log-derivatives as in the usual composition of normalizing flow layers. Parameters are learned directly (not output by a neural network).

Unlike affine transformations, where stacking K copies always reduces to a single scalar affine map, our nonlinear bijections gain expressivity with depth. Section 5.1 demonstrates monotonic improvement in KL divergence as K increases from 3 to 256. We found that mixing bijection types (e.g., alternating cubic rational and sinh) can improve performance, though single-type stacks already perform well.

4.2 Coupling Flows

As described in section 2.2, coupling layers partition coordinates into “active” and “passive” subsets. The passive coordinates are held fixed while a neural network (the *conditioner*) maps them to parameters of a bijection applied to the active coordinates.

Our analytic bijections serve as drop-in replacements for the affine transformations of Real NVP [1] or the monotonic splines of Neural Spline Flows [2]. Given passive coordinates \mathbf{x}_{pass} , a conditioner network g_ϕ outputs bijection parameters $\theta = g_\phi(\mathbf{x}_{\text{pass}})$, and active coordinates transform as $y_{\text{act},i} = h(x_{\text{act},i}; \theta_i)$. The log-Jacobian is simply $\sum_i \log |h'(x_{\text{act},i}; \theta_i)|$.

Training stability. While theoretically straightforward, coupling layers with expressive bijections require careful initialization [25, 26]. For Real NVP, this can be addressed by applying tanh as final coupling network activation to restrict affine scale parameters, and initializing the network close to zero. Even then, training can become unstable if the learning rate is not chosen to be sufficiently small. To improve stability when using our analytic bijections, we suppress initial deviations from identity, as mentioned in Section 3.3.2. These modifications ensure the flow begins near the identity transformation, preventing early training instabilities. More details are provided in Appendix A.4. Section 5.3 demonstrates that with appropriate parametrization, our bijections match or exceed spline performance on a 2D benchmark.

4.3 Radial Flows

We now introduce a novel flow architecture based on radial decomposition. The key idea is to decompose space into radial and angular components, applying our analytic bijections only to the radius while preserving the angular structure. This *direct parametrization*—where bijection parameters are learned as model weights rather than generated by a conditioner network—yields favorable properties: training stability, interpretability, and guaranteed smoothness of the learned density.

4.3.1 Radial decomposition

Any point $\mathbf{x} \in \mathbb{R}^n \setminus \{\mathbf{0}\}$ can be written as $\mathbf{x} = r\hat{\mathbf{x}}$, where $r = \|\mathbf{x}\|$ is the radius and $\hat{\mathbf{x}} = \mathbf{x}/r$ is the unit direction vector. A *radial transformation* applies a scalar bijection $f : \mathbb{R}_{\geq 0} \rightarrow \mathbb{R}_{\geq 0}$ to the radius while preserving direction:

$$g(\mathbf{x}) = f(r) \hat{\mathbf{x}} = \frac{f(\|\mathbf{x}\|)}{\|\mathbf{x}\|} \mathbf{x}. \quad (19)$$

This maps spheres to spheres, with the transformation strength controlled by the scalar bijection f . For regularity at the origin, we require $f(0) = 0$.

Jacobian. The log-determinant of the Jacobian has a simple closed form. For $\mathbf{x} = r\hat{\mathbf{x}}$ with $r > 0$, we have:

$$\log |\det J_g(\mathbf{x})| = \log |f'(r)| + (n-1) \log \left| \frac{f(r)}{r} \right|. \quad (20)$$

The first term is the usual 1D Jacobian of f . The second term arises from the $(n-1)$ -dimensional sphere: as f stretches or compresses the radius, the volume element on each sphere scales accordingly.

A straight-forward way to see this is to note that the absolute Jacobian determinant $|\det J|$ measures the change in volume $|\det J|$ induced by the transformation $r \mapsto R = f(r)$, and is given by the ratio between the volume elements $r^{n-1} dr d\Omega$ and $R^{n-1} dR d\Omega$. As the angular part $d\Omega$ remains unchanged, and we get

$$|\det J_g| = \left| \left(\frac{R}{r} \right)^{n-1} \frac{\partial R}{\partial r} \right|. \quad (21)$$

An alternative derivation can be found in Appendix [A.2](#).

Parametrization. We train the parameters of the radial flow layers directly as follows:

- **A center** $\mathbf{c} \in \mathbb{R}^n$: the transformation is applied relative to $\mathbf{x} - \mathbf{c}$.
- **A scaling vector** $\mathbf{s} \in \mathbb{R}_{>0}^n$: optional per-dimension scaling before computing r .
- **A scalar bijection** f : any of our analytic bijections from Section [3](#).

The full transformation becomes $g(\mathbf{x}) = \mathbf{c} + (f(r)(\mathbf{x} - \mathbf{c})) / r$, where $r = \|\mathbf{s} \odot (\mathbf{x} - \mathbf{c})\|$. The scaling factors \mathbf{s} cancel in the Jacobian, so [\(20\)](#) still applies.

Origin constraint. Since our analytic bijections f from Section [3](#) are defined on all of \mathbb{R} , they do not automatically satisfy $f(0) = 0$. We enforce this constraint by a simple correction: given any bijection f , we use $\tilde{f}(r) = f(r) - f(0)$. This ensures $\tilde{f}(0) = 0$ while preserving bijectivity and smoothness. Furthermore, this preserves the derivative: $\tilde{f}'(r) = f'(r)$. The Jacobian term $\tilde{f}(r)/r$ then approaches $\tilde{f}'(0) = f'(0)$ as $r \rightarrow 0$ by L'Hôpital's rule, ensuring the log-determinant remains well-defined everywhere. When stacking multiple scalar bijections within a single radial layer (Section [4.3.2](#)), the correction can be applied after each bijection or once after the full composition; we use the former but observe no significant difference.

4.3.2 Stacking radial layers

Expressivity comes from two levels of composition:

Multiple centers. We compose L radial layers, each with a distinct center \mathbf{c}_ℓ and scale \mathbf{s}_ℓ . Different centers enable the flow to create multiple “focal points” around which the density concentrates or spreads. Section [5.4](#) shows that increasing the number of centers monotonically improves performance^{[3](#)}.

³For a very large number of bijection layers, while expressivity increases, training may become less stable, requiring lower learning rates, careful initialization, or additional restriction of parameter ranges.

Stacked scalar bijections. Within each radial layer, the scalar bijection f can itself be a composition $f = f_K \circ \dots \circ f_1$ of multiple analytic bijections. This mirrors the 1D stacking of Section 4.1 and provides more expressivity for the radial transformation.

4.3.3 Relation to prior work

Radial flows were introduced by Rezende and Mohamed [21] for variational inference, using transformations of the form

$$r' = r + r \frac{\beta}{\alpha + r}, \quad \alpha, \beta \in \mathbb{R}. \quad (22)$$

This is a two-parameter family with limited expressivity.

Our radial flows build on this foundation substantially. First, for the radial bijection, we compose multiple expressive analytic bijections, not a single simple transformation. Second, we use multiple centers: many radial layers with learned centers, not a single origin. Third, we introduce angular dependence to enable direction-dependent stretching.

4.3.4 Properties and advantages

Training stability. Radial flows exhibit exceptional training stability compared to coupling flows. We routinely train with learning rates of 10^{-2} (on maximum likelihood loss functions), an order of magnitude larger than typical for coupling architectures. This stability arises from the geometric constraint: even with multiple layers, radial transformations do not tend to “cross” particle paths as much as coupling layers generically do, preventing the extreme Jacobians that can destabilize the latter.

Interpretability. The layer-by-layer action of radial flows is geometrically intuitive: each layer stretches or compresses the density radially around its center. This enables direct visualization of how the flow transforms the base distribution (see Section 5.2), providing insight into the learned representation.

Smoothness. Radial flows composed of smooth scalar bijections yield globally smooth densities. There are no piecewise constructions or domain boundaries as in spline-based methods. Figure 4 illustrates how a trained angular-dependent radial flow (Section 4.4) transforms concentric circles into spiral structure while preserving the non-crossing property.

Geometric constraints. The same structure that provides stability also imposes limitations. A single radial layer preserves rays: probability mass can be redistributed *along* rays from the center but not *between* them. Consequently, the angular distribution of mass (as viewed from the center) is conserved. For a single-center flow to approximate a target, the target’s angular mass distribution must approximately match the prior’s.

Stacking multiple radial layers with different centers mitigates this constraint: composing radial flows effectively enables angular redistribution (see Figure 8 of Section 5.2). However, the number of layers required may scale badly with dimension, and in contrast to coupling layers which update a large number of degrees of freedom per layer, the radial transformations are necessarily sequential.

4.4 Angular-Dependent Radial Flows

A natural extension allows the radial bijection to depend on the angular direction:

$$g(\mathbf{x}) = f(r, \hat{\mathbf{x}}) \hat{\mathbf{x}}, \quad (23)$$

where $f : \mathbb{R}_{\geq 0} \times S^{n-1} \rightarrow \mathbb{R}_{\geq 0}$ now depends on the unit vector $\hat{\mathbf{x}}$. This enables direction-dependent stretching while still preserving the radial structure.

Jacobian formula. The log-Jacobian formula (20) remains valid:

$$\log |\det J_g(\mathbf{x})| = \log \left| \frac{\partial f}{\partial r}(r, \hat{\mathbf{x}}) \right| + (n-1) \log \left| \frac{f(r, \hat{\mathbf{x}})}{r} \right|. \quad (24)$$

The angular dependence does not introduce additional Jacobian terms. To see this, we again consider the change in the volume element $r^{n-1} dr d\Omega$ induced by the transformation $r \mapsto R = f(r, \Omega)$. Note that $\hat{\mathbf{x}}$ is just an alternative way to denote the angular coordinates Ω . The Jacobian is upper-triangular as the off-diagonal element $d\Omega / dr = 0$ vanishes. Hence, the determinant is simply

$$\det J_g = (R/r)^{n-1} \det \begin{pmatrix} \partial R / \partial r & \partial \Omega / \partial r \\ \partial R / \partial \Omega & \partial \Omega / \partial \Omega \end{pmatrix} = (R/r)^{n-1} \frac{\partial R}{\partial r}. \quad (25)$$

Conditioning network. To implement angular dependence, a small network $g_\phi : S^{n-1} \rightarrow \mathbb{R}^p$ maps the unit vector $\hat{\mathbf{x}}$ to parameters $\theta = g_\phi(\hat{\mathbf{x}})$ of the scalar bijection. This can be a lightweight MLP, a convolutional network, or, in 2D, a Fourier expansion in the angle (Section 4.5).

Smoothness at the origin. A subtlety arises near $r = 0$: the unit vector $\hat{\mathbf{x}} = \mathbf{x} / \|\mathbf{x}\|$ is constant along rays, so the angular dependence of f “does not know” when we approach the origin. Since $g(\mathbf{x}) = (f(r, \hat{\mathbf{x}})/r) \mathbf{x}$, the linear approximation near the origin is

$$g(\mathbf{x}) \approx \frac{\partial f}{\partial r}(0, \hat{\mathbf{x}}) \cdot \mathbf{x}. \quad (26)$$

If $\partial_r f(0, \hat{\mathbf{x}})$ varies with $\hat{\mathbf{x}}$, this linear approximation depends on the approach direction, making g continuous but *not differentiable* at the origin. For full smoothness, we require

$$\frac{\partial f}{\partial r}(0, \hat{\mathbf{x}}) = 1 \quad \text{for all } \hat{\mathbf{x}}. \quad (27)$$

This ensures $f(r, \hat{\mathbf{x}})/r \rightarrow 1$ uniformly, so g is tangent to the identity at the origin regardless of the angular dependence at $r > 0$.

Enforcing $\partial_r f(0) = 1$ requires modifying the bijection, e.g., by composing with a correction term whose parameters are chosen to compensate. In practice, we find that for many target distributions, relaxing this constraint causes no instability, as the origin (or a collection of points if multiple layers are used) is a null set carrying negligible probability, and the angular dependence near it does not tend to vary rapidly.

Expressivity vs. stability tradeoff. Although angular-dependent radial flows are more expressive, they sometimes suffer from reduced training stability. In cases where the target’s structure permits, the angle-independent variant may be preferable, though it typically requires more centers and scales worse to high dimensions. It is important to note that a single radial layer leaves the marginal angular distribution, $p(\hat{\mathbf{x}}) = \int p(r, \hat{\mathbf{x}}) dr$, invariant. Therefore, multiple layers are required whenever the target and prior angular distributions do not align relative to a single center.

4.5 Radial Fourier Flows: Interpretable 2D Flows

In two dimensions, the angular direction $\hat{\mathbf{x}} \in S^1$ can be represented by a single angle $\phi \in (-\pi, \pi]$ as $\phi = \text{atan2}(x_2, x_1)$. This enables an explicit, interpretable parametrization of angular dependence via Fourier series.

Fourier expansion. We parametrize the bijection parameters as truncated Fourier series in ϕ :

$$\theta_j(\hat{\mathbf{x}}) = a_{j,0} + \sum_{k=1}^{(K-1)/2} [a_{j,k} \cos(k\phi) + b_{j,k} \sin(k\phi)], \quad (28)$$

where j indexes the parameters of the underlying scalar bijection (e.g., γ, α, β for cubic rational). The Fourier coefficients $\{a_{j,k}, b_{j,k}\}$ are learned directly.

Few-parameter expressivity. A modest number of Fourier terms yields rich angular structure. For example, with $K = 3$ and a single sinh bijection (5 parameters), the total parameter count is approximately $K \cdot 5 = 15$ for angular dependence, plus parameters for center and scale. Section 5.4 demonstrates that even the constant term ($K = 1$, 49 total parameters) captures significant structure, while $K = 3$ (319 parameters) produces detailed spiral patterns. See in particular Figure 12.

Interpretability. The Fourier representation provides direct insight into how the flow adapts to the target distribution:

- $a_{j,0}$ controls the isotropic (angle-independent) component.
- $a_{j,1}, b_{j,1}$ introduce dipole-like asymmetry.
- Higher harmonics capture finer angular structure.

Unlike neural network conditioners, the learned Fourier coefficients can be directly inspected and visualized, revealing which angular modes the flow uses to match the target.

Limitations. This explicit Fourier parametrization is specific to 2D. In higher dimensions, one could use spherical harmonics, but the number of basis functions grows rapidly. For general high-dimensional problems, the ResNet conditioning of Section 4.4 or coupling architectures (Section 4.2) are more practical, and would likely have to be combined with angle-transforming bijections or used as part of a stack with multiple centers.

5 Experiments

We evaluate our analytic bijections and flow architectures across four settings: one-dimensional density estimation, two-dimensional coupling and radial flows, and a physics application to lattice field theory. All experiments are implemented in JAX [27], and the analytic bijections presented in this work are available in the `bijx`⁴ library [28].

⁴<https://github.com/mathisgerdes/bijx>

Metrics. We use three complementary metrics to assess flow quality:

- **Reverse KL divergence** $D_{\text{KL}}(q\|p)$: The training objective, measuring how well the flow q covers the target p . Computed using the change-of-variables formula with Monte Carlo samples from the flow.
- **Forward KL divergence** $D_{\text{KL}}(p\|q)$: Measures how well the flow matches the target, penalizing missing modes more heavily than reverse KL. For density estimation experiments (Section 5.3), this reduces to negative log-likelihood plus the (estimated) target entropy.
- **Effective Sample Size (ESS)**: When the target density is known analytically, ESS quantifies how representative samples from the flow are for estimating expectations under the target. Defined as $\text{ESS} = (\sum_i w_i)^2 / \sum_i w_i^2$ where $w_i = p(x_i)/q(x_i)$ are importance weights. If this is evaluated on samples from the trained model, as is typically done, note that this is not sensitive to mode missing (see also Section 5.5).

Target distributions. We use target distributions that highlight different aspects of flow expressivity:

- **1D oscillating polynomial**: A hand-crafted univariate density with multiple modes and varying scales, designed to test the ability of stacked bijections to capture complex structure.
- **2D spiral**: A continuous spiral distribution in two dimensions, providing a challenging test case that requires capturing curved, non-convex structure. This distribution has significant radial organization, making it suitable for both coupling and radial flow evaluation.
- **2D Gaussian mixture**: A mixture of 5 Gaussians arranged in a circular pattern, testing the ability to capture well-separated modes. This multimodal target complements the unimodal spiral.
- **ϕ^4 lattice field theory**: A physics-motivated target on a 20×20 lattice with periodic boundary conditions, testing the scalability to higher dimensions and the ability to handle bimodal structure arising from spontaneous symmetry breaking.

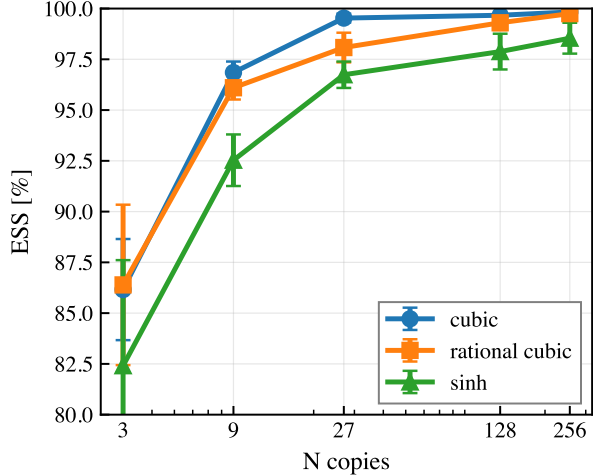
See Appendix B.3 for precise definitions of the synthetic distributions; Section 5.5 provides the ϕ^4 action.

Optimization. All models are trained using Adam with default momentum parameters ($\beta_1 = 0.9$, $\beta_2 = 0.999$). Learning rates and training schedules vary by experiment; details are provided in Appendix B.1. For each configuration, we report results averaged over 6 independent runs with different random seeds, with error bars indicating one standard deviation.

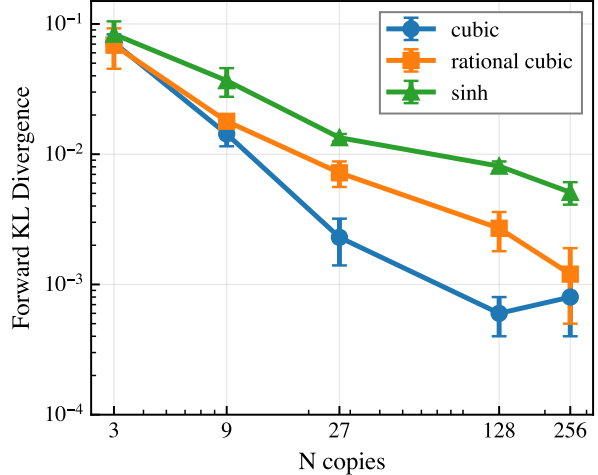
5.1 1D Density Estimation

We first evaluate our bijections in the simplest setting: one-dimensional flows constructed by stacking multiple scalar bijections (Section 4.1). This setting isolates the expressivity of the bijections themselves, without the confounding factors from neural network conditioners.

Experimental design. We train flows with $K \in \{3, 9, 27, 128, 256\}$ stacked bijections on the 1D oscillating polynomial target. Parameters are optimized using reverse KL divergence as the training loss. We compare all three bijection types: cubic polynomial, cubic rational, and sinh.



(a) Effective Sample Size (higher is better)



(b) Forward KL divergence (lower is better)

Figure 2: 1D flow performance vs. number of stacked bijections. Both metrics tend to improve with more bijections, with cubic polynomial performing best overall. Error bars show one standard deviation over 6 random seeds.

Results. Figure 2 shows ESS and forward KL divergence as a function of the number of stacked bijections. All three bijection types exhibit monotonic improvement with increasing K : ESS rises from approximately 82–86% at $K = 3$ to near 100% at $K = 256$, while forward KL drops from 6×10^{-2} to below 10^{-3} .

The cubic polynomial bijection consistently achieves the best performance, particularly at intermediate values of K . At $K = 27$, cubic reaches ESS $\approx 99\%$ and forward KL $\approx 3.5 \times 10^{-3}$, compared to $\approx 98\%$ and 7×10^{-3} for rational cubic, and $\approx 97\%$ and 1.5×10^{-2} for sinh.

Training dynamics. Figure 3 shows the evolution of reverse KL divergence during training. All configurations exhibit stable training behavior. The benefit of additional bijections is clearly visible: more copies lead to both faster initial convergence and lower final loss values.

Notably, the training dynamics are similar across bijection types, suggesting that the performance differences in Figure 2 arise from representational capacity rather than optimization difficulty. All three bijection types are equally easy to train in this setting.

Discussion. These results establish that our analytic bijections can effectively approximate complex 1D distributions when composed in sufficient depth. Unlike affine transformations—where stacking provides no additional expressivity (a composition of affine linear maps is a single affine linear map)—our nonlinear bijections genuinely benefit from depth. The monotonic improvement with K suggests that each additional bijection contributes incrementally to the flow’s representational capacity.

The strong performance of the cubic polynomial bijection may be attributed to its balanced parametrization: it has four parameters (γ, δ, a, b) providing sufficient flexibility while remaining well-behaved across its parameter space.

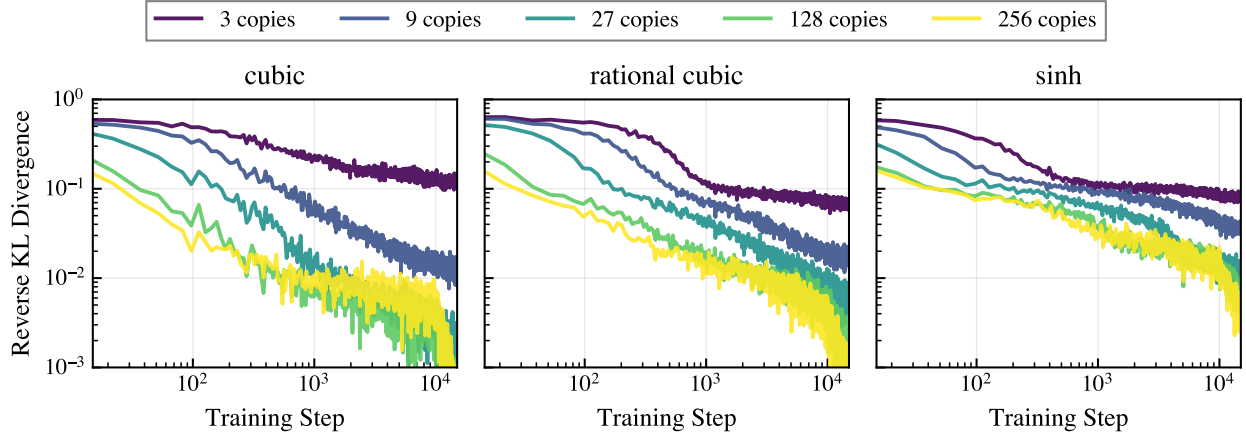


Figure 3: Training dynamics for 1D flows. Each panel shows reverse KL divergence vs. training steps for one bijection type, with different colors indicating the number of stacked bijections. All configurations converge stably, with more bijections generally achieving lower final loss.

5.2 2D Qualitative Analysis: Radial Flows

Beyond quantitative metrics, our radial flows offer qualitative advantages in interpretability and smoothness. This section visualizes how radial flows transform distributions, contrasting with standard coupling flows.

Geometric constraints of radial flows. A radial flow preserves rays: points along direction \hat{x} from the center remain at that angle after transformation. This means the total probability mass in any angular wedge is conserved; a radial flow can redistribute mass *along* rays but not *between* them. For a single-center radial flow to approximate a target distribution, the target’s angular distribution of mass (as viewed from the center) must approximately match the prior’s.

For the spiral target used in this section, a single center suffices: the spiral arm winds around the origin, so every angular direction intersects the arm roughly equally. The total mass per angular wedge is approximately uniform, matching the isotropic Gaussian prior. The angular-dependent bijection then concentrates mass *onto* the spiral along each ray. In general, multiple layers of (angular-dependent) radial transformations may be needed. Stacking radial layers with different centers enables effective “angular mixing” through composition (cf. the GMM experiment below).

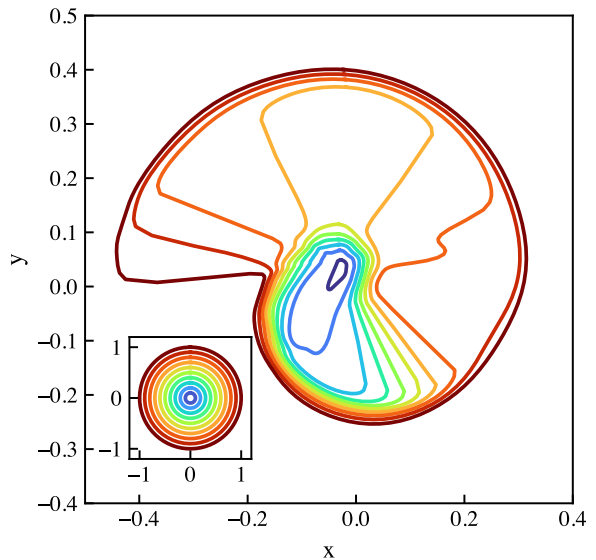


Figure 4: Transformation of points on a circle under a learned angular-dependent radial flow. Concentric circles (inset) transform smoothly into the spiral target structure. The color gradient indicates original radius, highlighting the preservation of radial ordering: paths never cross.

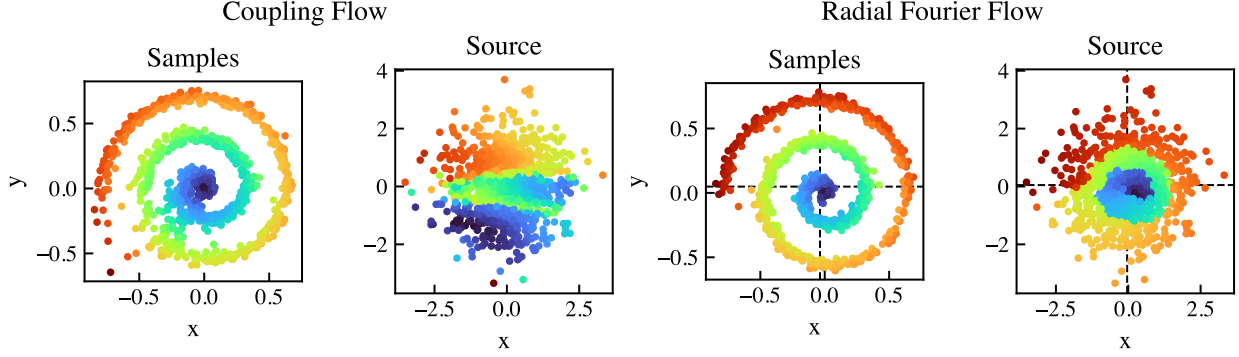


Figure 5: Source distribution samples and where they are mapped to by the trained coupling flow (left pair) and radial Fourier flow (right pair). Colors indicate position of samples in the target spiral. The radial flow preserves radial structure in the source, while the coupling flow mixes the radial structure.

Circle transformations. Figure 4 visualizes how a trained radial Fourier flow transforms concentric circles centered at the origin. The inset shows the original circles in the base distribution; the main plot shows their images under the learned flow. The circles deform smoothly into the spiral structure of the target, with paths that never cross—a geometric consequence of the radial architecture. This non-crossing property ensures that nearby points in the base distribution remain nearby after transformation, contributing to the smoothness of learned densities.

Source distribution comparison. Figure 5 compares the “source” distributions (inverse images of target samples) for a coupling flow versus our radial Fourier flow. Both flows successfully map their respective source distributions to the target spiral (left columns). However, the source distributions reveal fundamentally different transformation strategies.

The radial flow source exhibits clear radial organization: points near the spiral center (blue) remain near the origin in the source, while points on outer turns (red) lie at larger radii. In contrast, the coupling flow source shows mixing of colors arising from the alternating coordinate-wise transformations inherent to coupling layers. This visualization demonstrates that radial flows preserve geometric structure that coupling flows mix.

Density evolution during training. Figure 6 compares how the learned density evolves during training for both architectures. The radial Fourier flow (top row) develops a smooth, clean spiral structure that becomes progressively sharper and more detailed. By 5000 training steps, the density closely matches the target with no major artifacts.

To verify that centers need not be prescribed in advance, we deliberately initialize the radial flow center at $(-0.5, -1)$, far from the spiral’s natural center. At step 200, the non-smooth point where the angular dependence fails to be differentiable (since we do not enforce $\partial_r f(0) = 1$; cf. Section 4.4) is visible in the lower-left quadrant, indicating the current center location. By step 1000 this point has migrated close to the origin, and the final learned center (indicated by the crosshairs in Figure 5) lies very close to, but slightly offset from, the origin.

The coupling flow (bottom row) also converges to a spiral pattern, but exhibits distinctive artifacts: compressed thin lines of high probability, arising from the “folding” that the iterative coupling layers of affine transformations perform. While both flows achieve comparable log-likelihood scores (Section 5.3), the radial flow produces visibly smoother densities.

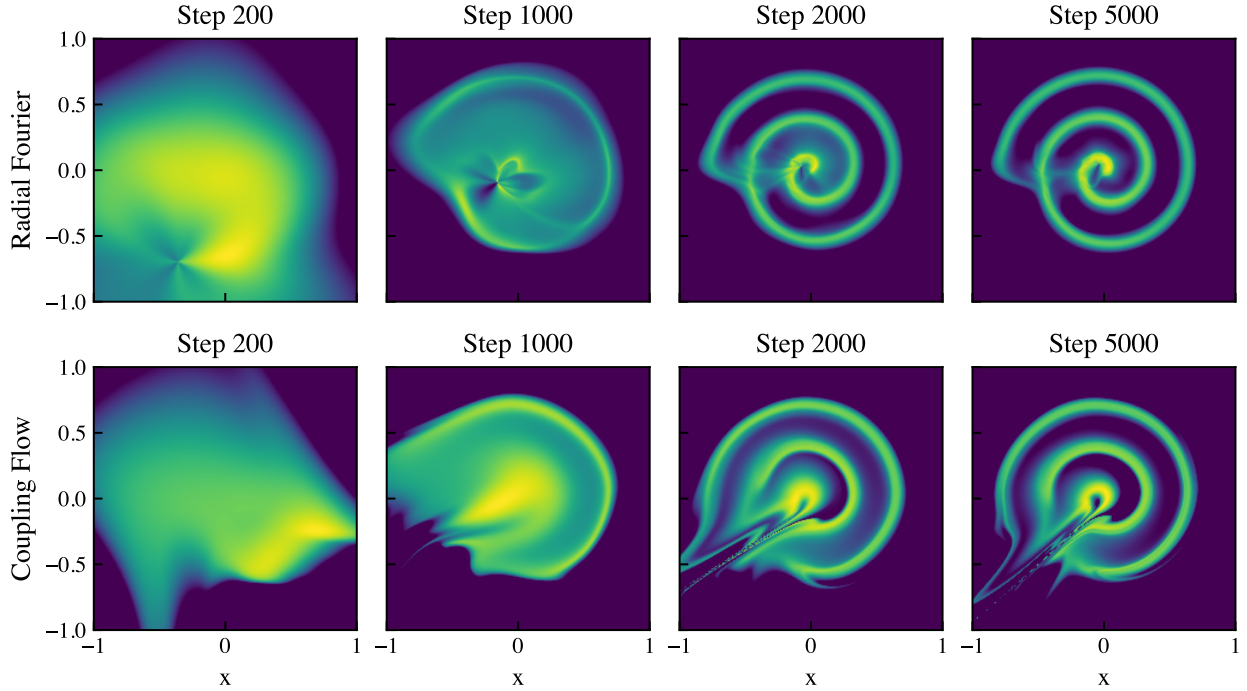


Figure 6: Evolution of learned log-likelihood during training. Top: Radial Fourier flow develops smooth spiral structure. Bottom: Coupling flow (Real NVP) converges to similar pattern but exhibits more artifacts. Both flows were trained for 5000 steps but lower learning rates for the coupling flow to avoid instability.

Layer-by-layer visualization. Figure 7 shows the progression through the 12 layers of a trained coupling flow (Real NVP). The alternation between horizontal and vertical transformations is clearly visible: odd layers transform along one axis while even layers transform along the perpendicular axis. The spiral structure emerges gradually through this sequence of axis-aligned operations.

This visualization illustrates why coupling flows produce the artifacts seen in Figure 6: the flow must approximate a smooth spiral through discrete, axis-aligned steps, similar to a kind of “folding”. In contrast, radial flows transform the distribution radially at each layer, more naturally matching the geometry of this target.

Multimodal distributions. The spiral distribution, while challenging, is topologically connected and has the approximate angular uniformity that allows a single-center radial flow to succeed. To test whether radial flows maintain their smoothness advantages when multiple centers are necessary, we train on a 2D Gaussian mixture model with 5 components arranged in a circle. Here, each mode occupies a narrow angular wedge with many directions containing almost no target mass, and thus violating the angular uniformity that a single-center flow requires. We therefore use 32 centers, enabling the stacked radial layers to effectively redistribute angular probability. Figure 8 compares three architectures, all using cubic bijections, isolating the effect of architectural choice from bijection type.

The pure radial flow (1.6k parameters) achieves the closest visual match to the target: smooth, circular blobs that faithfully reproduce the Gaussian components. The coupling flow (2311k parameters)—despite having over 1000 \times more parameters—produces the most distorted approx-

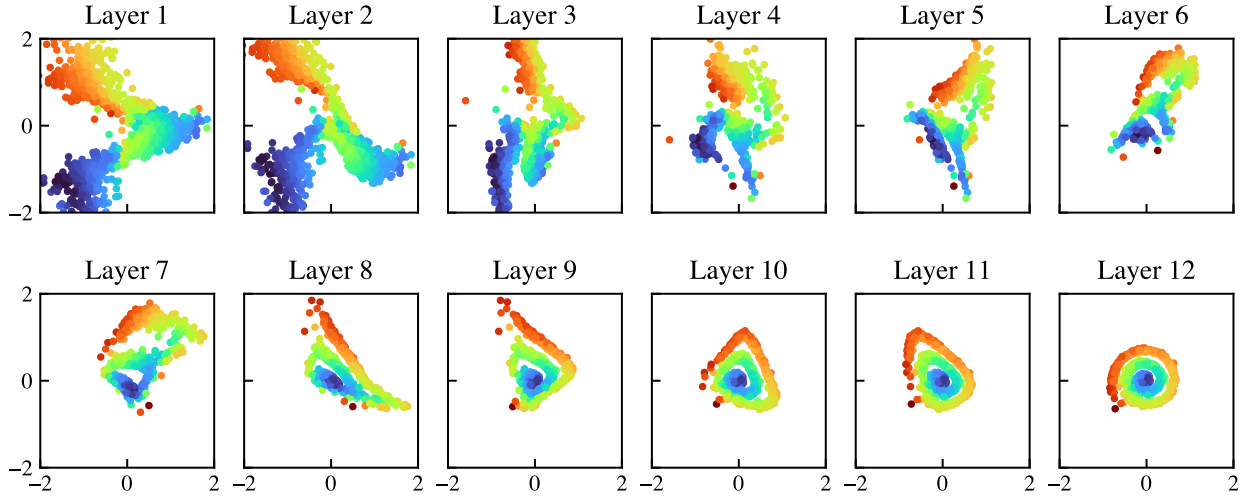


Figure 7: Layer-by-layer progression through a 12-layer coupling flow. Colors show final location in target distribution. Alternating axis-aligned transformations gradually build the spiral structure.

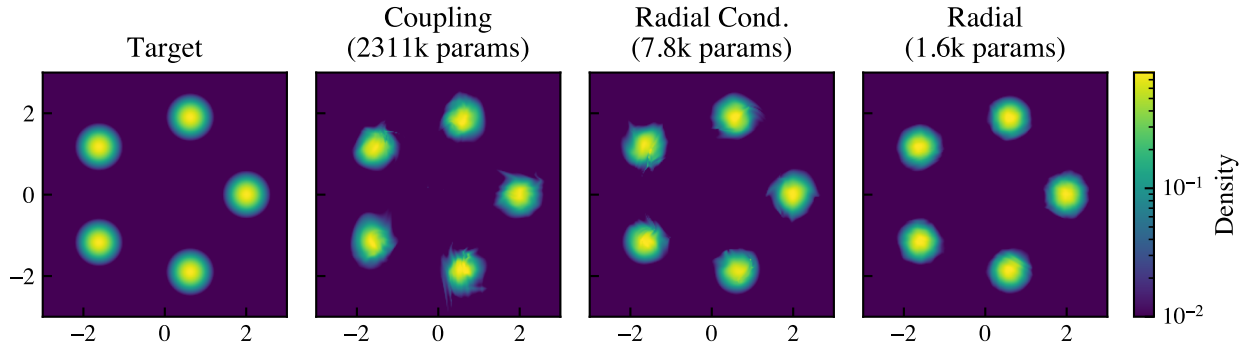


Figure 8: Learned densities for a 2D Gaussian mixture (5 components). All flows use cubic bijections. The pure radial flow (1.6k params) best reproduces the smooth, circular target blobs. The coupling flow (2311k params) exhibits spiky artifacts despite $1000\times$ more parameters. Color scale shows the log density to highlight the tail behavior of the learned distribution.

imation, with visible ‘‘spiky’’ artifacts on the blob boundaries. The angle-conditioned radial flow (7.8k parameters) provides an intermediate result: smoother than coupling but with faint streaks.

This comparison reinforces two conclusions: (1) the smoothness advantages of radial flows extend beyond unimodal distributions to well-separated modes, provided sufficient centers are used to overcome angular distribution constraints; (2) for targets with natural radial or circular structure, radial flows achieve excellent approximations with dramatically fewer parameters than coupling alternatives.

5.3 Coupling Layer Integration

We next evaluate our bijections as drop-in replacements for affine and spline transformers in coupling flows, demonstrating their practical applicability to standard architectures.

Experimental design. We train coupling flows on the 2D spiral distribution using forward KL divergence (negative log-likelihood) as the training objective. We stack $N \in \{1, 3, 9, 27\}$ copies of our scalar bijections within each coupling layer, testing whether additional bijection depth improves coupling flow performance. We compare against two baselines:

- **Affine** (Real NVP): Standard scale-and-shift coupling with tanh-bounded parameters.
- **Spline**: Monotonic rational quadratic splines with 8 knots, domain manually tuned to cover the target distribution.

All methods use identical training parameters and the same basic coupling architecture (12 coupling layers with ResNet conditioners). The conditioner networks have fixed numbers of hidden dimensions, and only differing in their final output dimensions to match the number of parameters for each chosen stack of scalar bijections.

Quantitative results. Figure 9 shows forward KL divergence for all methods. The affine baseline achieves $\text{KL} \approx 0.8$; the spline baseline achieves $\text{KL} \approx 0.45$.

Our analytic bijections achieve competitive or superior performance. At $N = 9$ copies, the cubic polynomial bijection achieves the best performance ($\text{KL} \approx 0.35$), outperforming both baselines. The sinh bijection also performs well at $N = 9$ ($\text{KL} \approx 0.5$), matching the spline baseline. The rational cubic bijection shows more variable performance, achieving good results at $N = 3$ but degrading at $N = 27$, likely due to training dynamics that may be resolvable by tuning hyperparameters.

Training dynamics. Figure 10 compares training curves across methods. All configurations show stable convergence, though with different final loss values. Our bijections with $N \geq 9$ copies achieve lower training loss ($\text{KL} \approx 0.2\text{--}0.4$) than the affine (≈ 0.8) or spline (≈ 0.4) baselines, suggesting they more efficiently fit the training distribution.

5.4 Radial Flow Performance

We now evaluate the radial flow architecture introduced in Section 4.3, demonstrating its scaling behavior and the interpretability of the Fourier variant.

Experimental design. We train angle-independent radial flows on the 2D spiral distribution, varying two hyperparameters:

- **Number of centers** $L \in \{5, 10, 20, 40\}$: The number of radial layers, each with a learned center \mathbf{c}_ℓ .

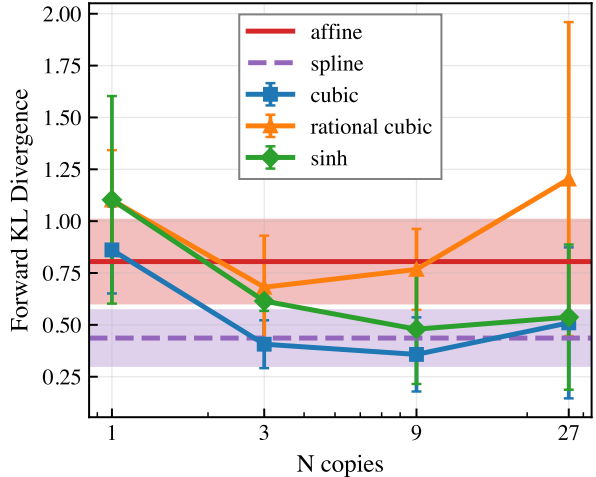


Figure 9: Forward KL divergence for 2D coupling flows. Our bijections (markers with error bars) improve with more copies up to $N = 9$, with cubic outperforming both affine and spline baselines (horizontal lines). Error bars show one standard deviation over 6 random seeds.

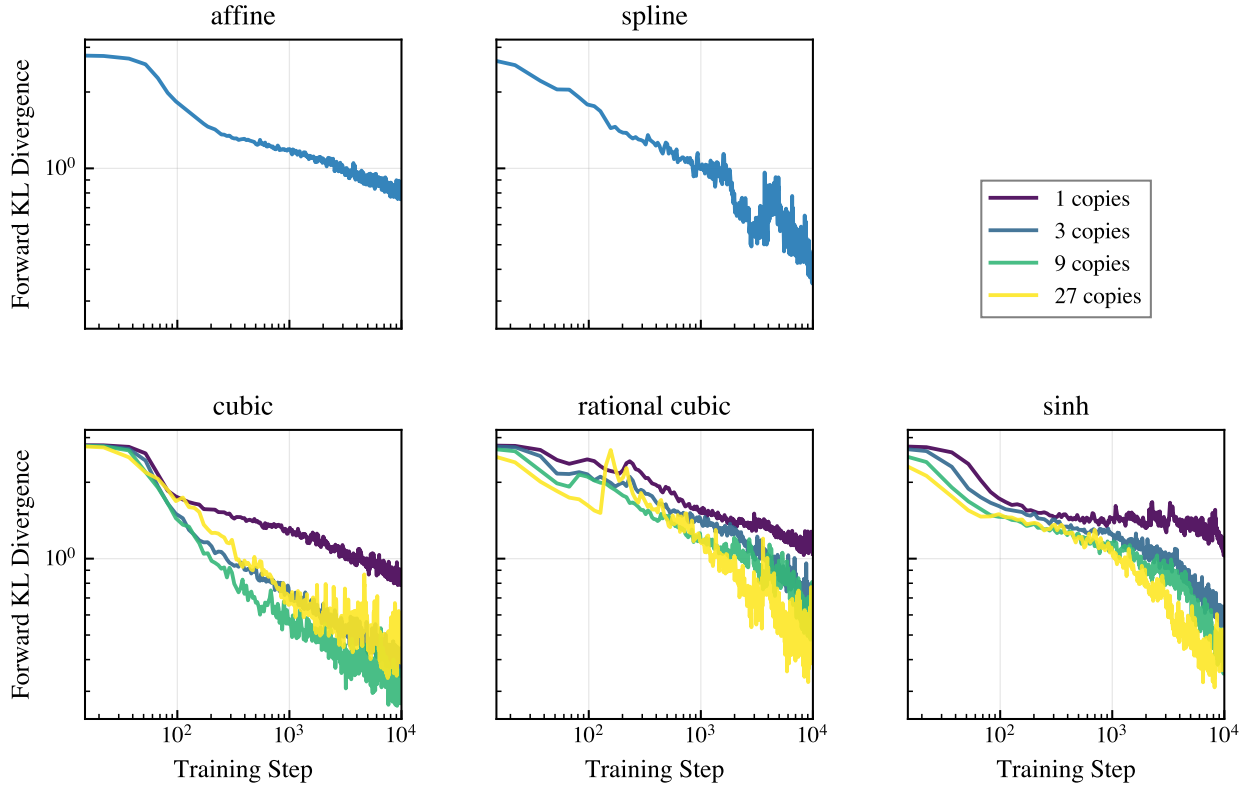


Figure 10: Training dynamics for 2D coupling flows. Each panel shows forward KL vs. training steps. Our methods (cubic, rational cubic, sinh) achieve lower or similar training loss compared to affine and spline baselines with sufficiently many stacked bijections.

- **Number of copies** $K \in \{1, 2, 8, 16, 32\}$: The number of stacked bijections within each radial layer.

All three bijection types are evaluated.

Scaling behavior. Figure 11 shows forward KL divergence as a function of both hyperparameters for each bijection type. All three architectures exhibit consistent scaling: performance tends to improve with both more centers (moving down rows) and more copies per center (moving right across columns), although too many copies may make training less stable.

At 40 centers with 16–32 copies, all bijection types achieve forward KL below 0.2, comparable to the best coupling flow results (Section 5.3). The cubic and rational cubic bijections achieve optimal performance around $K = 16$ copies, while sinh continues improving up to $K = 32$. Notably, even modest configurations (10 centers, 8 copies) achieve reasonable performance ($\text{KL} \approx 0.4$), demonstrating that radial flows can work well without extensive hyperparameter tuning.

Training stability. A key practical advantage of radial flows is their exceptional training stability (see table 3 in the appendix). We can train with learning rates of between one and two orders of magnitude larger than for coupling layers, without observing training instability.

Fourier flow interpretability. For the angular-dependent variant (Section 4.5), the Fourier parametrization enables direct inspection of learned angular structure. Figure 12 shows learned

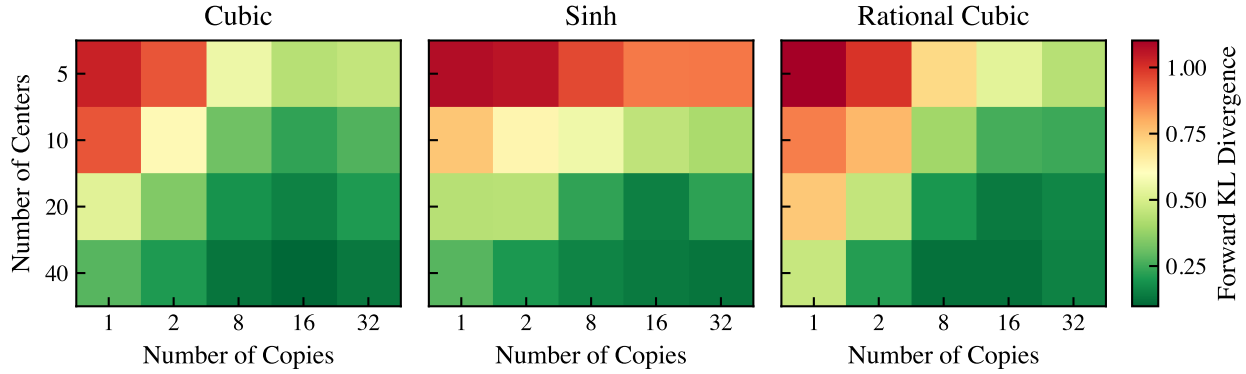


Figure 11: Forward KL divergence for radial flows as a function of number of centers and stacked bijections per center. All three bijection types show consistent improvement with both hyperparameters. Green indicates better performance.

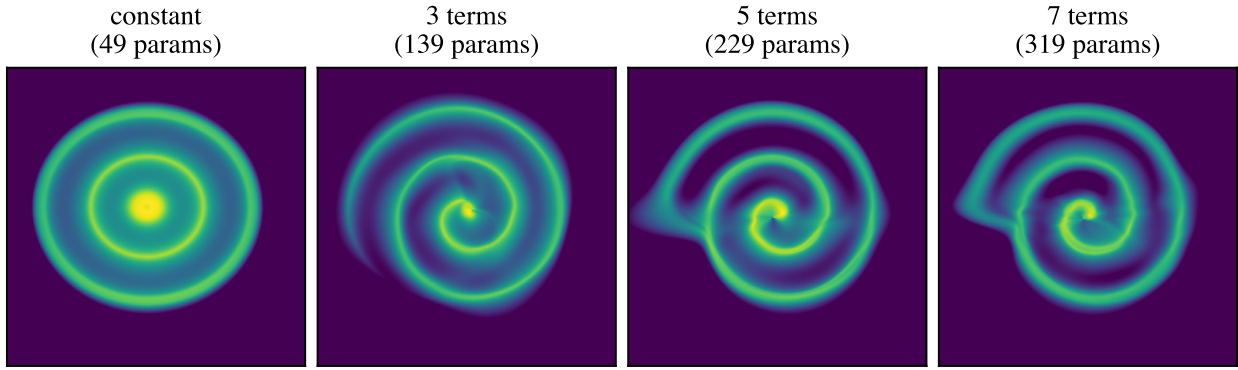


Figure 12: Learned densities for Fourier radial flows with increasing angular resolution. Even with only 49 parameters (constant term), the flow captures radial structure. Adding Fourier terms progressively reveals spiral detail, achieving high fidelity with just 319 parameters.

densities for a single-center radial flow with increasing numbers of Fourier terms. With only the zero-frequency term, the flow naturally produces concentric rings, with a spiral pattern emerging as higher frequencies are added.

This progression demonstrates two key properties:

- **Interpretability:** Each Fourier term has clear geometric meaning—the constant term captures radial structure, first-order terms introduce asymmetry, higher-order terms add finer angular detail. Unlike neural network conditioners, the learned transformation can be directly visualized. Figure 13 shows how $f(r, \phi)$ varies across input radius and angle, making explicit the effect of adding angular modes to the flow.
- **Transparency through simplicity:** With only 49–319 parameters (compared to millions in neural conditioners in typical Real NVP architectures), one can directly inspect what the model has learned rather than treating it as a black box.

Comparison with coupling flows. Comparing Figures 11 and 9, radial flows achieve similar quantitative performance to coupling flows on this 2D benchmark. However, radial flows offer distinct advantages:

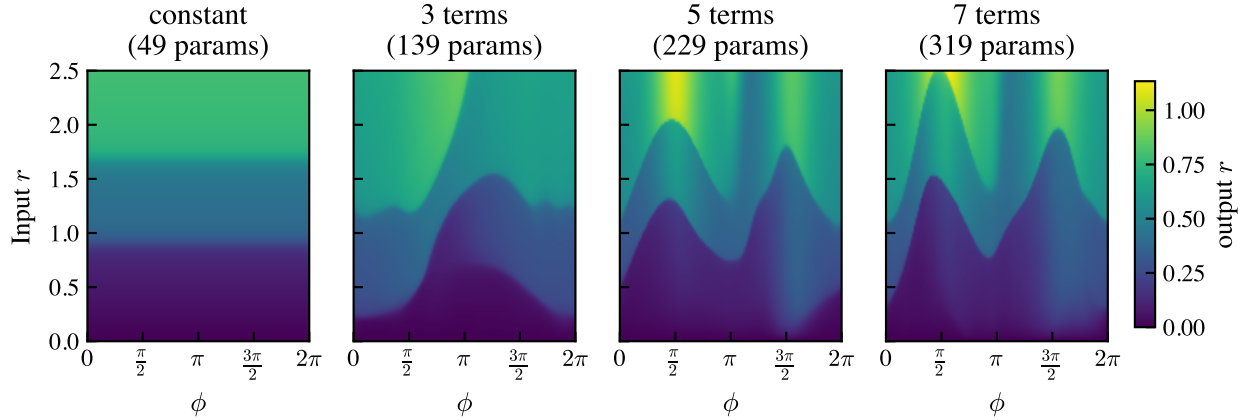


Figure 13: Radial transformation $f(r)$ as a function of input radius r (y-axis) and angle ϕ (x-axis) for models with increasing Fourier terms. Color indicates output radius $r' = f(r, \phi)$. With one term (constant), the transformation is independent of ϕ , yielding vertical color bands.

- Superior training stability (higher learning rates, no divergence).
- Interpretable transformations (Section 5.2).
- Smoother learned densities with fewer artifacts.
- Faster training and inference, and can easily be combined with coupling layers.

These properties make radial flows an attractive choice for low-dimensional problems or applications where interpretability and smoothness matter.

5.5 Physics Application: Lattice Field Theory

To demonstrate that our analytic bijections scale to higher-dimensional problems, we apply them to sampling from the ϕ^4 scalar field theory on a two-dimensional lattice. Normalizing flows have emerged as a promising tool for accelerating Monte Carlo simulations in lattice field theory, where traditional Markov chain methods suffer from critical slowing down near phase transitions (for a recent review, see e.g. Kanwar [29] and Cheng and Stratikopoulou [30]). In what follows we consider one of the simplest quantum field theories—the scalar field theory with quartic interactions.

Theory setup. We consider the ϕ^4 theory on a 20×20 square lattice with periodic boundary conditions. The lattice action, which gives the target distribution is $p(\phi) \propto \exp(-S[\phi])$, is

$$S[\phi] = \sum_x \left[\sum_{\mu=1}^2 (\phi_{x+\hat{\mu}} - \phi_x)^2 + m^2 \phi_x^2 + \lambda \phi_x^4 \right], \quad (29)$$

where x indexes lattice sites, $\hat{\mu}$ denotes unit vectors in each spatial direction, and the sum over μ captures nearest-neighbor interactions with periodic wrapping. We fix $m^2 = -4$ (negative mass squared creates a double-well potential at each site) and vary the quartic coupling λ to explore different physical regimes.

We present two experiments demonstrating complementary approaches to how the analytic bijections we present here can be used: (1) comparing bijection architectures within a standard

coupling flow as originally explored in this context by Albergo, Kanwar, and Shanahan [31], and (2) using problem-specific design to prevent mode collapse in the bimodal regime.

5.5.1 Bjection comparison in coupling flows

For larger λ (we use $\lambda = 4.807$), the kinetic and quartic coupling terms dominate and the distribution is effectively unimodal, with correlation length $\xi \approx L/4$ at this lattice size. This regime tests whether our analytic bijections improve upon affine linear baselines in a standard coupling architecture.

Architecture. We use a coupling flow with 12 layers, each employing a small convolutional network (2 hidden layers, 16 channels, 3×3 kernels with circular padding) to predict bijection parameters from masked sites. The flow includes an initial *Fourier scaling* component: a linear transformation in Fourier space that rescales each momentum mode,

$$\tilde{\phi}_k \mapsto e^{s_{|k|}} \tilde{\phi}_k, \quad (30)$$

where $\tilde{\phi}_k$ denotes the Fourier transform of the field and $s_{|k|}$ is a learnable parameter, shared across all modes with the same momentum magnitude $|k|$ as is consistent with the 90° rotation and reflection symmetries of the lattice. Independent of the bijections used in the coupling layers, we find this simple scaling significantly improves training by allowing the flow to match the target's momentum-dependent variance structure.

We compare four configurations: affine-only (Real NVP baseline), and three variants where each coupling layer applies a stack of 8 analytic bijections followed by an affine linear transformation.

Results. Figure 14 shows the effective sample size (ESS) during training. All three analytic bijection types—cubic, sinh, and rational cubic—significantly outperform the affine baseline, achieving ESS of above 40% compared to around or below 35% for affine linear (Real NVP).

This demonstrates that our bijections provide meaningful improvements in a higher-dimensional setting where the target distribution has genuine physical structure.

5.5.2 Preventing mode collapse via problem-specific design

For smaller λ , the correlation length grows and the distribution becomes bimodal. The key observable is the *magnetization*,

$$M = \frac{1}{L^2} \sum_x \phi_x, \quad (31)$$

which measures the spatially-averaged field value. When the negative mass term dominates over the quartic coupling, typical field configurations cluster around one of two minima at $\phi \approx \pm v_0$, yielding a bimodal distribution in M with

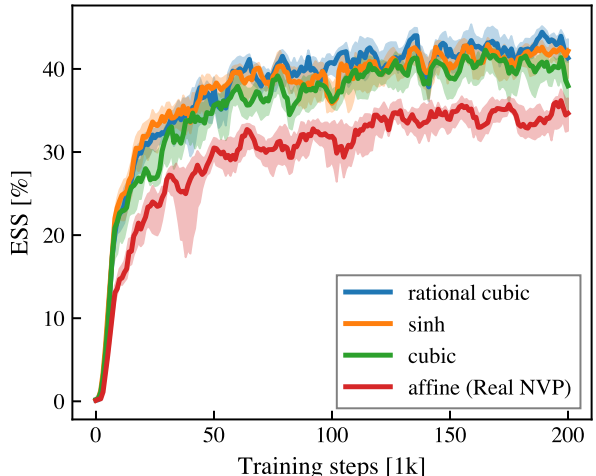


Figure 14: ESS during training for ϕ^4 theory on a 20×20 lattice. Analytic bijections (cubic, sinh, rational cubic) achieve around 10% higher ESS than the affine baseline. Median with interquartile range (shaded region) over 3 runs, smoothed with 5-step moving average.

peaks at approximately $\pm v_0$. Standard training often collapses to a single mode, missing half of the distribution. This experiment demonstrates how problem-specific architectural choices can prevent mode collapse.

\mathbb{Z}_2 symmetry. The ϕ^4 action (29) is invariant under the global \mathbb{Z}_2 transformation $\phi \rightarrow -\phi$. On finite lattices, there is no true spontaneous symmetry breaking—both modes should be sampled equally. However, coupling flows trained with reverse KL divergence tend to collapse to one mode, as the loss does not penalize missing modes that receive no probability mass from the model. Note that this is also not captured by the ESS as monitored during training, since again one typically uses samples from the trained model itself.

Architecture modification. We modify the architecture to easily express strong bimodality while preserving \mathbb{Z}_2 symmetry via a *zero-mode bijection*: a stack of 8 cubic bijections applied to the spatially-averaged field $\tilde{\phi}_0$ (the $k = 0$ Fourier mode) before the coupling layers. To preserve the symmetry, the bijection is applied to $|\tilde{\phi}_0|$, preserving the sign of $\tilde{\phi}_0$. Just as for the radial bijections above the bijection is constrained to preserve the original, and \mathbb{R}_+ gets mapped to \mathbb{R}_+ . Note that we already apply FFT (fast Fourier transform) for the Fourier-scaling layer. Otherwise, The zero-mode bijection could easily be applied without the cost of a Fourier transform by applying it as:

$$\phi_x \mapsto \phi_x - M_\phi + f(M_\phi), \quad (32)$$

where f is the scalar bijection and M_ϕ is the magnetization (mean) of the field configuration ϕ .

Training strategy. We compare two approaches:

- **Naive:** Train the full model (FFT scaling + coupling layers) from random initialization for 100k steps.
- **Pretrain:** First train only the FFT scaling and zero-mode bijection for 100k steps (coupling layers frozen), then resume training the full model for another 100k steps.

Results. Figures 15 and 16 show training dynamics and final magnetization distributions. The naive approach achieves high ESS ($\approx 90\%$) but this is *misleading*: 100% of samples have negative magnetization throughout training, indicating complete mode collapse. The pretrain approach maintains exactly 50% negative magnetization during pretraining (as required by the \mathbb{Z}_2 -symmetric zero-mode bijection), and crucially *preserves* this balance when coupling layers are activated. The final ESS reaches similarly high values as the naive approach, but now with both modes correctly sampled.

Figure 17 visualizes this mode collapse directly: samples from the naive approach (top row) are uniformly dark (negative field values), while samples from the pretrain approach (middle and bottom rows) alternate between positive and negative configurations.

5.6 Discussion

We summarize the key findings across our experiments and discuss their implications.

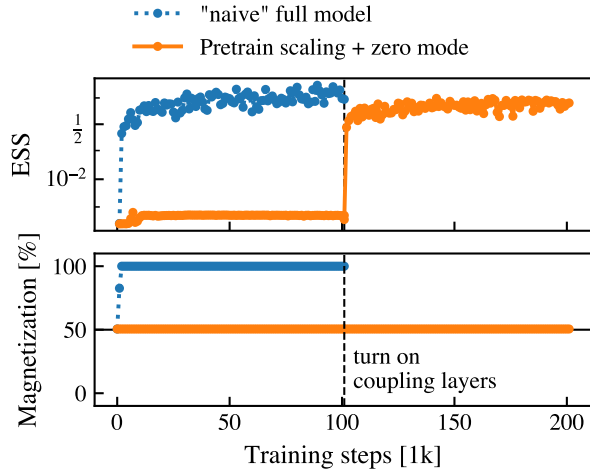


Figure 15: Training dynamics for bimodal ϕ^4 distribution. **Top:** ESS (log scale). **Bottom:** Fraction of samples with negative magnetization. Naive training achieves high ESS but collapses to one mode (100% negative). Pretraining the zero-mode bijection maintains balanced sampling (50%) while achieving the same final ESS. Vertical dashed line marks when coupling layers are activated for the pretrain approach.

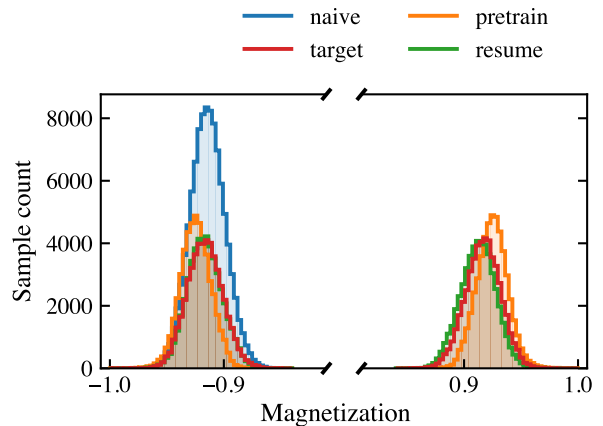


Figure 16: Magnetization histograms after training (100k samples). The “naive” model collapses to a single mode. After pretraining, the model already captures the bimodal structure. After resuming training, each mode closely matches the target distribution of the magnetization (unbiased samples obtained via MCMC).

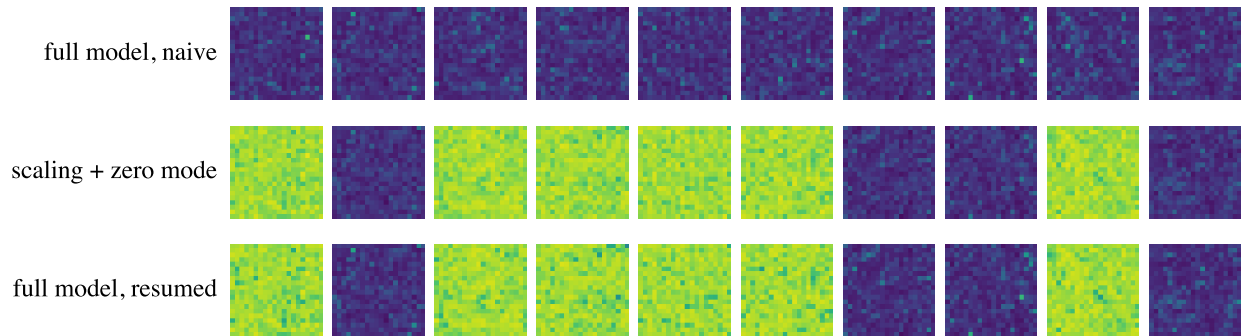


Figure 17: Lattice field configurations from trained models with 10 samples per row and same random seeds per column. **Top:** Naive training produces only negative-magnetization configurations (blue). **Middle:** After pretraining the zero-mode bijection, samples alternate between positive (yellow/green) and negative modes (blue). **Bottom:** Resumed training with coupling layers preserves bimodal sampling.

Bijection effectiveness. All three analytic bijections successfully approximate complex distributions when composed in sufficient depth. While application dependent, in our tests the cubic polynomial often performs best, likely due to its balanced four-parameter structure. The sinh bijection, while slightly less performant, offers the unique capability of global shift via its μ, ν parameters. The rational cubic bijection performs well in 1D, shows higher variance in coupling flows, but yields the best results on the ϕ^4 experiment.

Architecture comparison. Our experiments reveal complementary strengths of coupling and radial architectures. Coupling flows excel at high-dimensional problems where their coordinate-wise factorization enables tractable computation; our ϕ^4 experiments (Section 5.5) validate this scaling on a 20×20 lattice. Recent theoretical work [32] proves distributional universality for well-conditioned coupling flows. Radial flows are preferable for lower-dimensional problems where smoothness, interpretability, or simplicity are priorities. In practice, it may be beneficial to combine two or more architectural approaches, possibly including several training steps as explored in the ϕ^4 experiment.

Smoothness and artifacts. The qualitative analysis (Section 5.2) reveals that radial flows produce fundamentally smoother learned densities than coupling flows. For applications requiring smooth densities, such as force matching in molecular simulation, where smoothness of $\nabla \log p$ is critical, this difference may be significant.

Limitations. Our evaluation has several limitations that future work should address:

- **Dimensionality:** While our ϕ^4 experiments demonstrate analytic flows can be applied in high dimensional coupling flows, radial flows as presented here remain limited to low dimensions where the “shell” structure of spheres is tractable. Systematic benchmarks on intermediate-dimensional problems (e.g., 10–100D) would further characterize the scaling behavior.
- **Target diversity:** Although we evaluate on both unimodal (spiral) and multimodal (Gaussian mixture) targets, both have relatively simple structure. Performance on distributions with complex data-manifold topology or heavy tails remains to be characterized.
- **Hyperparameter sensitivity:** We did not extensively tune hyperparameters for each method, focusing instead on fair comparison under fixed settings. Each method could likely be improved with method-specific tuning.

6 Conclusion

We have introduced a family of *analytic bijections*, cubic rational, sinh, and cubic polynomial, that combine properties previously unavailable in a single construction: global smoothness, unbounded domain, closed-form inverses, and expressive parametrization supporting both local deformations and global redistribution of probability mass. These bijections serve as drop-in replacements for affine or spline transformers in coupling flows, achieving competitive or superior performance while guaranteeing smooth learned densities.

Beyond scalar bijections, we developed *radial flows*: a novel architecture based on polar decomposition that transforms radius while preserving angular direction. Radial flows can be directly

parametrized (no conditioner networks), exhibit exceptional training stability, and produce geometrically interpretable transformations. On 2D benchmarks, radial flows match coupling flow quality with orders of magnitude fewer parameters, while reducing or avoiding artifacts inherent to coordinate-wise coupling flow transformations. The Fourier variant demonstrates that complex distributions can be captured with as few as 50–300 learned parameters, yielding a high level of interpretability and training stability.

Our experiments on ϕ^4 lattice field theory (Section 5.5) demonstrate that coupling flows with our bijections scale to higher-dimensional problems with a physically relevant structure. On a 20×20 lattice, analytic bijections outperform affine baselines by around 10% in effective sample size. Moreover, problem-specific design—a \mathbb{Z}_2 -symmetric zero-mode bijection trained separately—prevents mode collapse in the bimodal regime, illustrating how expressive bijections enable architectural innovations tailored to the target distribution.

Limitations and future work. While our ϕ^4 experiments validate coupling flows on lattice field theory, radial flows remain limited to low dimensions. Several directions merit further investigation. First, hybrid architectures combining radial and coupling layers could leverage the strengths of both: radial layers for smooth, interpretable coarse structure and coupling layers for fine-grained corrections. Second, extending the Fourier parametrization to spherical harmonics would enable interpretable angular dependence in three dimensions, with potential applications to molecular and materials modeling.

Extensions to compact domains. The conjugation principle naturally extends to the unit interval $[0, 1]$ via logit-sigmoid bijections: using $g(x) = \log(x/(1-x))$, the conjugation $h(x) = g^{-1}(g(x) + \delta)$ yields the analytically invertible family $h(x) = x/(x + (1-x)e^{-\delta})$. However, this reduces to a well-known logistic transformation with limited expressivity. For the circle S^1 , Möbius transformations provide a natural family of smooth, analytically invertible bijections already explored by Rezende et al. [22].

Broader perspective. The design space for normalizing flows remains vast, with recent work exploring both strict constraints (exact analytic inverses) and relaxed constraints (free-form flows with numerical inversion [33]). Our work demonstrates that principled construction of scalar bijections—guided by smoothness, invertibility, and expressivity requirements—yields practical benefits across multiple architectures. While we focused on coupling flows, autoregressive flows share essentially the same structure—a conditioner network generating parameters for a scalar bijection—so our bijections apply there equally. We hope these tools prove useful to practitioners seeking smooth, stable, and interpretable density estimation.

Acknowledgments

We thank Julian Ebelt and Kim Nicoli for helpful discussions. The research of MG and MC is supported by the Vici grant (number VI.C.232.117) from the Dutch Research Council (NWO).

References

- [1] L. Dinh, J. Sohl-Dickstein, and S. Bengio. “Density Estimation Using Real NVP”. In: *5th International Conference on Learning Representations, ICLR 2017, Toulon, France, April 24-26, 2017, Conference Track Proceedings*. 2017. arXiv: [1605.08803 \[cs.LG\]](https://arxiv.org/abs/1605.08803).

[2] C. Durkan, A. Bekasov, I. Murray, and G. Papamakarios. “Neural Spline Flows”. In: *Advances in Neural Information Processing Systems*. Vol. 32. Curran Associates, Inc., 2019. arXiv: [1906.04032 \[stat.ML\]](https://arxiv.org/abs/1906.04032).

[3] C.-W. Huang, D. Krueger, A. Lacoste, and A. Courville. “Neural Autoregressive Flows”. In: *Proceedings of the 35th International Conference on Machine Learning*. International Conference on Machine Learning. PMLR, July 3, 2018, pp. 2078–2087. arXiv: [1804.00779 \[cs.LG\]](https://arxiv.org/abs/1804.00779).

[4] R. T. Q. Chen and D. K. Duvenaud. “Neural Networks with Cheap Differential Operators”. In: *Advances in Neural Information Processing Systems*. Vol. 32. Curran Associates, Inc., 2019. arXiv: [1912.03579 \[cs.LG\]](https://arxiv.org/abs/1912.03579).

[5] J. Behrmann, W. Grathwohl, R. T. Q. Chen, D. Duvenaud, and J.-H. Jacobsen. “Invertible Residual Networks”. In: *Proceedings of the 36th International Conference on Machine Learning*. International Conference on Machine Learning. PMLR, May 24, 2019, pp. 573–582. arXiv: [1811.00995 \[cs.LG\]](https://arxiv.org/abs/1811.00995).

[6] J. Ho, X. Chen, A. Srinivas, Y. Duan, and P. Abbeel. “Flow++: Improving Flow-Based Generative Models with Variational Dequantization and Architecture Design”. In: *Proceedings of the 36th International Conference on Machine Learning, ICML 2019, 9-15 June 2019, Long Beach, California, USA*. Ed. by K. Chaudhuri and R. Salakhutdinov. Vol. 97. Proceedings of Machine Learning Research. PMLR, 2019, pp. 2722–2730. arXiv: [1902.00275 \[cs\]](https://arxiv.org/abs/1902.00275).

[7] C. Meng, Y. Song, J. Song, and S. Ermon. “Gaussianization Flows”. In: *Proceedings of the Twenty Third International Conference on Artificial Intelligence and Statistics*. International Conference on Artificial Intelligence and Statistics. PMLR, June 3, 2020, pp. 4336–4345. arXiv: [2003.01941 \[cs.LG\]](https://arxiv.org/abs/2003.01941).

[8] J. Köhler, A. Krämer, and F. Noe. “Smooth Normalizing Flows”. In: *Advances in Neural Information Processing Systems*. Vol. 34. Curran Associates, Inc., 2021, pp. 2796–2809. arXiv: [2110.00351 \[stat.ML\]](https://arxiv.org/abs/2110.00351).

[9] E. G. Tabak and E. Vanden-Eijnden. “Density Estimation by Dual Ascent of the Log-Likelihood”. In: *Communications in Mathematical Sciences* 8.1 (Mar. 2010), pp. 217–233. ISSN: 1539-6746, 1945-0796.

[10] G. Papamakarios, E. Nalisnick, D. J. Rezende, S. Mohamed, and B. Lakshminarayanan. “Normalizing Flows for Probabilistic Modeling and Inference”. In: *J. Mach. Learn. Res.* 22.1 (Jan. 1, 2021), 57:2617–57:2680. ISSN: 1532-4435. arXiv: [1912.02762 \[stat\]](https://arxiv.org/abs/1912.02762).

[11] I. Kobyzhev, S. J. D. Prince, and M. A. Brubaker. “Normalizing Flows: An Introduction and Review of Current Methods”. In: *IEEE Trans. Pattern Anal. Machine Intell.* 43.11 (Nov. 1, 2021), pp. 3964–3979. doi: [10.1109/tpami.2020.2992934](https://doi.org/10.1109/tpami.2020.2992934). arXiv: [1908.09257 \[stat.ML\]](https://arxiv.org/abs/1908.09257).

[12] G. Papamakarios, I. Murray, and T. Pavlakou. “Masked Autoregressive Flow for Density Estimation”. In: *Advances in Neural Information Processing Systems 30: Annual Conference on Neural Information Processing Systems 2017, December 4-9, 2017, Long Beach, CA, USA*. Ed. by I. Guyon, U. von Luxburg, S. Bengio, H. M. Wallach, R. Fergus, S. V. N. Vishwanathan, and R. Garnett. 2017, pp. 2338–2347. arXiv: [1705.07057 \[stat.ML\]](https://arxiv.org/abs/1705.07057).

[13] D. P. Kingma, T. Salimans, R. Jozefowicz, X. Chen, I. Sutskever, and M. Welling. “Improved Variational Inference with Inverse Autoregressive Flow”. In: *Advances in Neural Information Processing Systems*. Vol. 29. Curran Associates, Inc., 2016. arXiv: [1606.04934](https://arxiv.org/abs/1606.04934). URL: <https://proceedings.neurips.cc/paper/2016/hash/ddeebdeefdb7e7e7a697e1c3e3d8ef54-Abstract.html>.

[14] L. Dinh, D. Krueger, and Y. Bengio. “NICE: Non-linear Independent Components Estimation”. In: *3rd International Conference on Learning Representations, ICLR 2015, San Diego, CA, USA, May 7-9, 2015, Workshop Track Proceedings*. Ed. by Y. Bengio and Y. LeCun. 2015. arXiv: [1410.8516 \[cs.LG\]](https://arxiv.org/abs/1410.8516).

[15] D. P. Kingma and P. Dhariwal. “Glow: Generative Flow with Invertible 1x1 Convolutions”. In: *Advances in Neural Information Processing Systems*. Vol. 31. Curran Associates, Inc., 2018. arXiv: [1807.03039 \[stat.ML\]](https://arxiv.org/abs/1807.03039).

[16] T. Q. Chen, J. Behrmann, D. Duvenaud, and J.-H. Jacobsen. “Residual Flows for Invertible Generative Modeling”. In: *Proceedings of the 33rd International Conference on Neural Information Processing Systems*. Ed. by H. M. Wallach, H. Larochelle, A. Beygelzimer, F. d’Alché-Buc, E. B. Fox, and R. Garnett. 2019, pp. 9913–9923. arXiv: [1906.02735 \[stat\]](https://arxiv.org/abs/1906.02735).

[17] R. T. Q. Chen, Y. Rubanova, J. Bettencourt, and D. K. Duvenaud. “Neural Ordinary Differential Equations”. In: *Advances in Neural Information Processing Systems*. Vol. 31. Curran Associates, Inc., 2018. arXiv: [1806.07366 \[cs\]](https://arxiv.org/abs/1806.07366).

[18] W. Grathwohl, R. T. Q. Chen, J. Bettencourt, I. Sutskever, and D. Duvenaud. “FFJORD: Free-Form Continuous Dynamics for Scalable Reversible Generative Models”. In: *7th International Conference on Learning Representations, ICLR 2019, New Orleans, LA, USA, May 6-9, 2019*. OpenReview.net, 2019. arXiv: [1810.01367 \[cs.LG\]](https://arxiv.org/abs/1810.01367).

[19] H. M. Dolatabadi, S. M. Erfani, and C. Leckie. “Invertible Generative Modeling Using Linear Rational Splines”. In: *The 23rd International Conference on Artificial Intelligence and Statistics, AISTATS 2020, 26-28 August 2020, Online [Palermo, Sicily, Italy]*. Ed. by S. Chiappa and R. Calandra. Vol. 108. Proceedings of Machine Learning Research. PMLR, 2020, pp. 4236–4246. arXiv: [2001.05168 \[stat\]](https://arxiv.org/abs/2001.05168).

[20] S. Hong and S. Y. Chun. “Neural Diffeomorphic Non-uniform B-spline Flows”. In: *Proceedings of the 37th AAAI Conference on Artificial Intelligence*. Ed. by B. Williams, Y. Chen, and J. Neville. AAAI Press, 2023, pp. 12225–12233. DOI: [10.1609/AAAI.V37I10.26441](https://doi.org/10.1609/AAAI.V37I10.26441). arXiv: [2304.04555 \[cs\]](https://arxiv.org/abs/2304.04555).

[21] D. J. Rezende and S. Mohamed. “Variational Inference with Normalizing Flows”. In: *Proceedings of the 32nd International Conference on Machine Learning, ICML 2015, Lille, France, 6-11 July 2015*. Ed. by F. R. Bach and D. M. Blei. Vol. 37. JMLR Workshop and Conference Proceedings. JMLR.org, 2015, pp. 1530–1538. arXiv: [1505.05770 \[stat.ML\]](https://arxiv.org/abs/1505.05770).

[22] D. J. Rezende, G. Papamakarios, S. Racanière, M. S. Albergo, G. Kanwar, P. E. Shanahan, and K. Cranmer. “Normalizing Flows on Tori and Spheres”. In: *Proceedings of the 37th International Conference on Machine Learning, ICML 2020, 13-18 July 2020, Virtual Event*. Vol. 119. Proceedings of Machine Learning Research. PMLR, 2020, pp. 8083–8092. arXiv: [2002.02428 \[stat.ML\]](https://arxiv.org/abs/2002.02428).

[23] L. I. Midgley, V. Stimper, J. Antorán, E. Mathieu, B. Schölkopf, and J. M. Hernández-Lobato. “SE(3) Equivariant Augmented Coupling Flows”. In: *Advances in Neural Information Processing Systems 36: Annual Conference on Neural Information Processing Systems 2023, NeurIPS 2023, New Orleans, LA, USA, December 10 - 16, 2023*. Ed. by A. Oh, T. Naumann, A. Globerson, K. Saenko, M. Hardt, and S. Levine. 2023. arXiv: [2308.10364 \[cs\]](https://arxiv.org/abs/2308.10364).

[24] F. Koehler, V. Mehta, and A. Risteski. “Representational Aspects of Depth and Conditioning in Normalizing Flows”. In: *Proceedings of the 38th International Conference on Machine Learning, ICML 2021, 18-24 July 2021, Virtual Event*. Ed. by M. Meila and T. Zhang. Vol. 139. Proceedings of Machine Learning Research. PMLR, 2021, pp. 5628–5636. arXiv: [2010.01155 \[cs\]](https://arxiv.org/abs/2010.01155).

[25] D. Andrade. *Stable Training of Normalizing Flows for High-dimensional Variational Inference*. Feb. 26, 2024. arXiv: [2402.16408 \[stat\]](https://arxiv.org/abs/2402.16408). Pre-published.

[26] S. Hong, I. Park, and S. Y. Chun. “On the Robustness of Normalizing Flows for Inverse Problems in Imaging”. In: *IEEE/CVF International Conference on Computer Vision, ICCV 2023, Paris, France, October 1-6, 2023*. IEEE, 2023, pp. 10711–10721. DOI: [10.1109/ICCV51070.2023.00986](https://doi.org/10.1109/ICCV51070.2023.00986). arXiv: [2212.04319 \[cs\]](https://arxiv.org/abs/2212.04319).

[27] J. Bradbury, R. Frostig, P. Hawkins, M. J. Johnson, C. Leary, D. Maclaurin, G. Necula, A. Paszke, J. Vander{P}las, S. Wanderman-{M}ilne, and Q. Zhang. *JAX: Composable Transformations of Python+NumPy Programs*. Version 0.3.13. jax-ml, 2018. URL: <https://github.com/jax-ml/jax>.

[28] M. Gerdes and M. C. N. Cheng. “Bijx: Bijections and Normalizing Flows with JAX/NNX”. In: *J. Open Source Softw.* 10.116 (Dec. 6, 2025), p. 9521. ISSN: 2475-9066. DOI: [10.21105/joss.09521](https://doi.org/10.21105/joss.09521).

[29] G. Kanwar. “Flow-Based Sampling for Lattice Field Theories”. In: *Proceedings of The 40th International Symposium on Lattice Field Theory — PoS(LATTICE2023)*. The 40th International Symposium on Lattice Field Theory. Fermi National Accelerator Laboratory: Sissa Medialab, Oct. 11, 2024, p. 114. DOI: [10.22323/1.453.0114](https://arxiv.org/abs/2401.01297). arXiv: [2401.01297 \[hep-lat\]](https://arxiv.org/abs/2401.01297).

[30] M. C. N. Cheng and N. Stratikopoulou. “Lecture Notes on Normalizing Flows for Lattice Quantum Field Theories”. In: *arXiv:2504.18126 [hep-lat]* (Apr. 25, 2025). arXiv: [2504.18126 \[hep-lat\]](https://arxiv.org/abs/2504.18126).

[31] M. S. Albergo, G. Kanwar, and P. E. Shanahan. “Flow-Based Generative Models for Markov Chain Monte Carlo in Lattice Field Theory”. In: *Phys. Rev. D* 100.3 (Aug. 23, 2019), p. 034515. ISSN: 2470-0010, 2470-0029. DOI: [10.1103/PhysRevD.100.034515](https://doi.org/10.1103/PhysRevD.100.034515). arXiv: [1904.12072 \[hep-lat\]](https://arxiv.org/abs/1904.12072).

[32] F. Draxler, S. Wahl, C. Schnörr, and U. Köthe. “On the Universality of Volume-Preserving and Coupling-Based Normalizing Flows”. In: *Proceedings of the 41st International Conference on Machine Learning*. Vol. 235. ICML’24. Vienna, Austria: JMLR.org, July 21, 2024, pp. 11613–11641.

[33] F. Draxler, P. Sorrenson, L. Zimmermann, A. Rousselot, and U. Köthe. “Free-Form Flows: Make Any Architecture a Normalizing Flow”. In: *Proceedings of The 27th International Conference on Artificial Intelligence and Statistics*. International Conference on Artificial Intelligence and Statistics. PMLR, Apr. 18, 2024, pp. 2197–2205. arXiv: [2310.16624 \[cs.LG\]](https://arxiv.org/abs/2310.16624).

Appendix

A Detailed Derivations

This appendix provides complete mathematical derivations for results stated in the main text. We cover the analytic inverse of the cubic rational bijection (Section A.1), Jacobian calculations for all bijection types and radial flows (Section A.2), and the parametrization schemes used for stable training (Section A.4).

A.1 Cubic Rational Bijection: Analytic Inverse

The cubic rational bijection (Eq. 12) is $y = h(x) = x + \lambda(x - \gamma)/(1 + (x - \gamma)^2/\sigma^2)$. Without loss of generality, set $\gamma = 0$ and define $\beta = 1/\sigma^2 > 0$, giving

$$y = x + \frac{\lambda x}{1 + \beta x^2}. \quad (33)$$

Reduction to cubic equation. Clearing denominators and rearranging yields

$$\beta x^3 - \beta y x^2 + (1 + \lambda)x - y = 0, \quad (34)$$

a general cubic with coefficients $a = \beta$, $b = -\beta y$, $c = 1 + \lambda$, $d = -y$.

Cardano's formula. For the general cubic $ax^3 + bx^2 + cx + d = 0$, the discriminants are $\Delta_0 = b^2 - 3ac$ and $\Delta_1 = 2b^3 - 9abc + 27a^2d$. For our coefficients,

$$\Delta_0 = \beta^2 y^2 - 3\beta(1 + \lambda), \quad \Delta_1 = -2\beta^3 y^3 + 9\beta^2 y(1 + \lambda) - 27\beta^2 y. \quad (35)$$

The real root is

$$x = -\frac{1}{3a} \left(b + C + \frac{\Delta_0}{C} \right) = \frac{\beta y - C - \Delta_0/C}{3\beta}, \quad (36)$$

where $C = \sqrt[3]{(\Delta_1 \pm \sqrt{\Delta_1^2 - 4\Delta_0^3})/2}$ with sign chosen to maximize $|C|$. Our parameter constraints $-1 < \lambda < 8$ and $\beta > 0$ ensure h is strictly increasing, guaranteeing a unique real solution.

Derivation of parameter bounds. Bijectivity requires $h'(x) = 1 + \lambda(1 - \beta x^2)/(1 + \beta x^2)^2 > 0$ for all x . Substituting $u = \beta x^2 \geq 0$ and defining $g(u) = (1 - u)/(1 + u)^2$, we find $g'(u) = (u - 3)/(1 + u)^3$ vanishes at $u = 3$ with $g(3) = -1/8$. Since $g(0) = 1$ and $g(u) \rightarrow 0^-$ as $u \rightarrow \infty$, we have $g(u) \in [-1/8, 1]$. Thus $h'(x) = 1 + \lambda g(u) > 0$ requires $1 - \lambda/8 > 0$ for $\lambda \geq 0$ and $1 + \lambda > 0$ for $\lambda < 0$, yielding $-1 < \lambda < 8$.

Numerical stability. The implementation avoids catastrophic cancellation by selecting the sign in $\Delta_1 \pm \sqrt{\Delta_1^2 - 4\Delta_0^3}$ that maximizes magnitude. The formula remains stable when $C \approx 0$ because this only occurs when $\Delta_0 \approx 0$ (nearly linear cubic).

A.2 Jacobian Derivations

A.2.1 Scalar bijection Jacobians

Cubic rational. For $h(x) = x + \lambda x/(1 + \beta x^2)$, the derivative is $h'(x) = 1 + \lambda(1 - \beta x^2)/(1 + \beta x^2)^2$. Under constraints $-1 < \lambda < 8$ and $\beta > 0$, we have $h'(x) > 0$ everywhere.

Sinh bijection. For $h(x) = \operatorname{arcsinh}(e^\mu(e^\nu \sinh(x) + \delta))$, the log-Jacobian is

$$\log h'(x) = \mu + \nu + \log \cosh(x) - \frac{1}{2} \log(1 + \arg^2), \quad (37)$$

where $\arg = e^\mu(e^\nu \sinh(x) + \delta)$. We use $\log \cosh(x) = |x| + \log(1 + e^{-2|x|}) - \log 2$ for numerical stability.

Cubic polynomial. For $h(x) = g^{-1}(g(x) + \delta)$ with $g(x) = ax + bx^3$, the chain rule gives $h'(x) = g'(x)/g'(h(x)) = (a + 3bx^2)/(a + 3bh(x)^2)$. We compute this via automatic differentiation.

A.2.2 Radial flow Jacobian

For $g(\mathbf{x}) = f(r)\hat{\mathbf{x}}$ where $r = \|\mathbf{x}\|$ and $\hat{\mathbf{x}} = \mathbf{x}/r$, we compute $\partial g_i / \partial x_j$ using $\partial r / \partial x_j = \hat{x}_j$ and $\partial \hat{x}_i / \partial x_j = (\delta_{ij} - \hat{x}_i \hat{x}_j)/r$:

$$\frac{\partial g_i}{\partial x_j} = \frac{\partial}{\partial x_j} (f(r)\hat{x}_i) = f'(r)\hat{x}_j \hat{x}_i + f(r) \cdot \frac{\delta_{ij} - \hat{x}_i \hat{x}_j}{r} = \frac{f(r)}{r} \delta_{ij} + \left(f'(r) - \frac{f(r)}{r} \right) \hat{x}_i \hat{x}_j. \quad (38)$$

In matrix form, $J = \frac{f(r)}{r} I + \left(f'(r) - \frac{f(r)}{r} \right) \hat{\mathbf{x}} \hat{\mathbf{x}}^T$. Applying the matrix determinant lemma

$$\det(\alpha I + \beta \mathbf{u} \mathbf{u}^T) = \alpha^{n-1}(\alpha + \beta) \quad (39)$$

for $\|\mathbf{u}\| = 1$:

$$\log |\det J| = \log |f'(r)| + (n-1) \log \left| \frac{f(r)}{r} \right|. \quad (40)$$

A.2.3 Angular-dependent radial flow Jacobian

For $g(\mathbf{x}) = f(r, \hat{\mathbf{x}})\hat{\mathbf{x}}$, the log-Jacobian formula remains

$$\log |\det J| = \log \left| \frac{\partial f}{\partial r} \right| + (n-1) \log \left| \frac{f(r, \hat{\mathbf{x}})}{r} \right|. \quad (41)$$

In spherical coordinates (r, Ω) , the transformation is $(r, \Omega) \mapsto (f(r, \Omega), \Omega)$ with $\det(J_{\text{sph}}) = \partial f / \partial r$. For the latter, note that the Jacobian in spherical coordinates is upper-triangular as $d\Omega / dr = 0$, so the determinant is the product of the diagonal terms and $d\Omega / d\Omega = 1$, leaving us with only the radial term. Via the chain rule, $J_{\text{Cart}} = J_{\text{sph} \rightarrow \text{Cart}}(f, \Omega) \cdot J_{\text{sph}} \cdot J_{\text{Cart} \rightarrow \text{sph}}(r, \Omega)$. The coordinate transformation determinants $\det(J_{\text{Cart} \rightarrow \text{sph}}) = 1/(r^{n-1} G(\Omega))$ and $\det(J_{\text{sph} \rightarrow \text{Cart}}) = f^{n-1} G(\Omega)$ contain a common angular factor $G(\Omega)$ that cancels, yielding

$$\det(J_{\text{Cart}}) = \left(\frac{f}{r} \right)^{n-1} \frac{\partial f}{\partial r}. \quad (42)$$

A.3 Numerical Implementation Details

The sinh bijection $h(x) = \sigma \cdot \operatorname{arcsinh}(e^\mu(e^\nu \sinh((x - \gamma)/\sigma) + \delta)) + \gamma$ involves nested exponentials requiring careful numerical treatment.

Asymptotic approximations. For $|x| > T = 15$, we use asymptotic forms: $h(x) \approx x + \sigma(\mu + \nu)$ (positive x) or $h(x) \approx x - \sigma(\mu + \nu)$ (negative x), with $\log h'(x) \approx 0$.

Stable special functions. We compute $\log \cosh(x) = |x| + \log(1 + e^{-2|x|}) - \log 2$ to avoid overflow for $|x| \gtrsim 710$. For $\frac{1}{2} \log(1 + z^2)$, we use $\frac{1}{2} \log 1p(z^2)$ when $|z|^2 < 10^8$ and $\log |z|$ otherwise.

A.4 Parametrization Details

We map unconstrained parameters $\theta_i \in \mathbb{R}$ to valid bijection parameters. For *coupling layers*, we suppress initial deviations from identity by scaling inputs to transforms (divide by 10) or zero-initializing conditioner weights, ensuring stable training and initialization of the normalizing flow close to the identity. If the conditioner network outputs are unsuppressed, the density defined by the normalizing flow at initialization would grow increasingly irregular with flow depth and destabilize training.

Cubic rational ($\epsilon_\alpha^{\text{low}} = \epsilon_\alpha^{\text{high}} = 10^{-3}$, $\epsilon_\beta = 10^{-1}$):

$$\begin{aligned} \gamma &= \theta_0, \\ \lambda &= \lambda_{\text{low}} + (\lambda_{\text{high}} - \lambda_{\text{low}}) \cdot \text{sigmoid} \left(\theta_1 + \text{logit} \left(\frac{-\lambda_{\text{low}}}{\lambda_{\text{high}} - \lambda_{\text{low}}} \right) \right), \\ \beta &= \epsilon_\beta + \text{softplus}(\theta_2 + 1), \end{aligned} \quad (43)$$

where $\lambda_{\text{low}} = -1 + \epsilon_\alpha^{\text{low}}$, $\lambda_{\text{high}} = 8 - \epsilon_\alpha^{\text{high}}$, and again $\beta = 1/\sigma^2$. The logit offset ensures $\theta_1 = 0 \Rightarrow \lambda = 0$.

Sinh ($\epsilon_\alpha = 0.1$):

$$\gamma = \theta_0, \quad \alpha = \text{softplus}(\theta_1) + \epsilon_\alpha, \quad \delta = \theta_2, \quad \mu = \text{arcsinh}(\theta_3), \quad \nu = \text{arcsinh}(\theta_4). \quad (44)$$

The arcsinh transform allows μ, ν to take large values while dampening growth.

Cubic polynomial ($\epsilon_a = \epsilon_b = 10^{-2}$):

$$\gamma = \theta_0, \quad \delta = \theta_1, \quad a = \epsilon_a + \text{softplus}(\theta_2), \quad b = \epsilon_b + \text{softplus}(\theta_3). \quad (45)$$

Design choices. Epsilon values (10^{-3} to 10^{-1}) ensure strict positivity for numerical stability and well-defined gradients. For bounded intervals, sigmoid with affine rescaling and logit offset ensures initialization close to the identity.

B Additional Experimental Results

B.1 Training Details

Table 3 summarizes the training hyperparameters used across experiments. All experiments use the Adam optimizer with default momentum parameters ($\beta_1 = 0.9$, $\beta_2 = 0.999$).

Exponential decay schedules decay learning rate by $10 \times$ over training; warmup linearly increases from 0 over 100 steps. The higher learning rates for radial flows (5×10^{-3} to 10^{-2}) vs. coupling flows (4×10^{-4}) reflect superior training stability.

Table 3: Training hyperparameters by experiment type.

Experiment	Steps	Batch	Learning Rate	Schedule
1D flows	15,000	128	10^{-3}	Exponential decay
2D coupling (spiral)	5,000	256	4×10^{-4}	Warmup (100 steps) + decay
2D radial (spiral)	10,000	128	5×10^{-3}	Constant
Fourier radial (spiral)	5,000	256	10^{-2}	Constant
2D GMM (radial flows)	5,000	256	10^{-2}	Constant
2D GMM (coupling)	5,000	256	5×10^{-4}	Warmup (100 steps) + decay
ϕ^4 coupling	100,000	64	10^{-3}	Constant

[†]Pretrain phase trains only FFT scaling and zero-mode bijection; coupling layers are frozen.

Architecture specifications. 2D coupling: 12 layers, alternating masks, 2-layer MLP conditioners (128 hidden units, GELU). All bijection types use identical conditioners for fair comparison. Radial flows: learned centers from $\mathcal{N}(0, 1)$, stacked scalar bijections; Fourier variants use near-zero initialized coefficients. GMM comparison: coupling (16 layers, 12 bijections/layer, 2311k params), angular radial (32 centers, 5 Fourier terms, 12 bijections/center, 7.8k params), pure radial (32 centers, 12 bijections/center, 1.6k params). ϕ^4 : 12 coupling layers with checkerboard masks, small ConvNets (2 layers, 16 channels, 3×3 kernels, circular padding), FFT per-shell scaling; realNVP+ uses 8 analytic + 1 affine bijection per layer; bimodal adds \mathbb{Z}_2 -symmetric zero-mode bijection (8 cubic bijections on $k = 0$).

B.2 Bijection Visualizations

Figure 18 shows parameter sweeps for each bijection type (columns: $f(x)$, $|f'(x)|$, resulting density from standard normal). Cubic rational creates localized bumps (λ, σ), sinh offers local deformation (δ) and global shift (μ), cubic polynomial provides similar capabilities (δ, a, b). Unlike affine transforms, these bijections create localized peaks, asymmetric stretching, and multi-modal structures when composed.

B.3 Target Distribution Specifications

1D oscillating polynomial. Unnormalized density: $\log p(x) = a_1 \sin(\omega_1 x) e^{-\gamma_1 x^2} + a_2 \cos(\omega_2 x) + a_4 x^4$, with $a_1 = 1$, $\omega_1 = 5$, $\gamma_1 = 5$, $a_2 = 2$, $\omega_2 = 10$, $a_4 = -0.2$.

2D spiral. Density-free sampling: $x = t \cos(t) \cdot s + \epsilon_x$, $y = t \sin(t) \cdot s + \epsilon_y$, where $t \sim \text{Uniform}(0, 5\pi)$, $s = 1/20$, $\epsilon_x, \epsilon_y \sim \mathcal{N}(0, 0.02^2)$ (2.5 turns).

2D Gaussian mixture. $p(x) = \frac{1}{K} \sum_{k=1}^K \mathcal{N}(x | \mu_k, \sigma^2 I)$ with $\mu_k = R(\cos(2\pi k/K), \sin(2\pi k/K))^T$. We use $K = 5$, $R = 2.0$, $\sigma = 0.2$ (pentagonal arrangement).

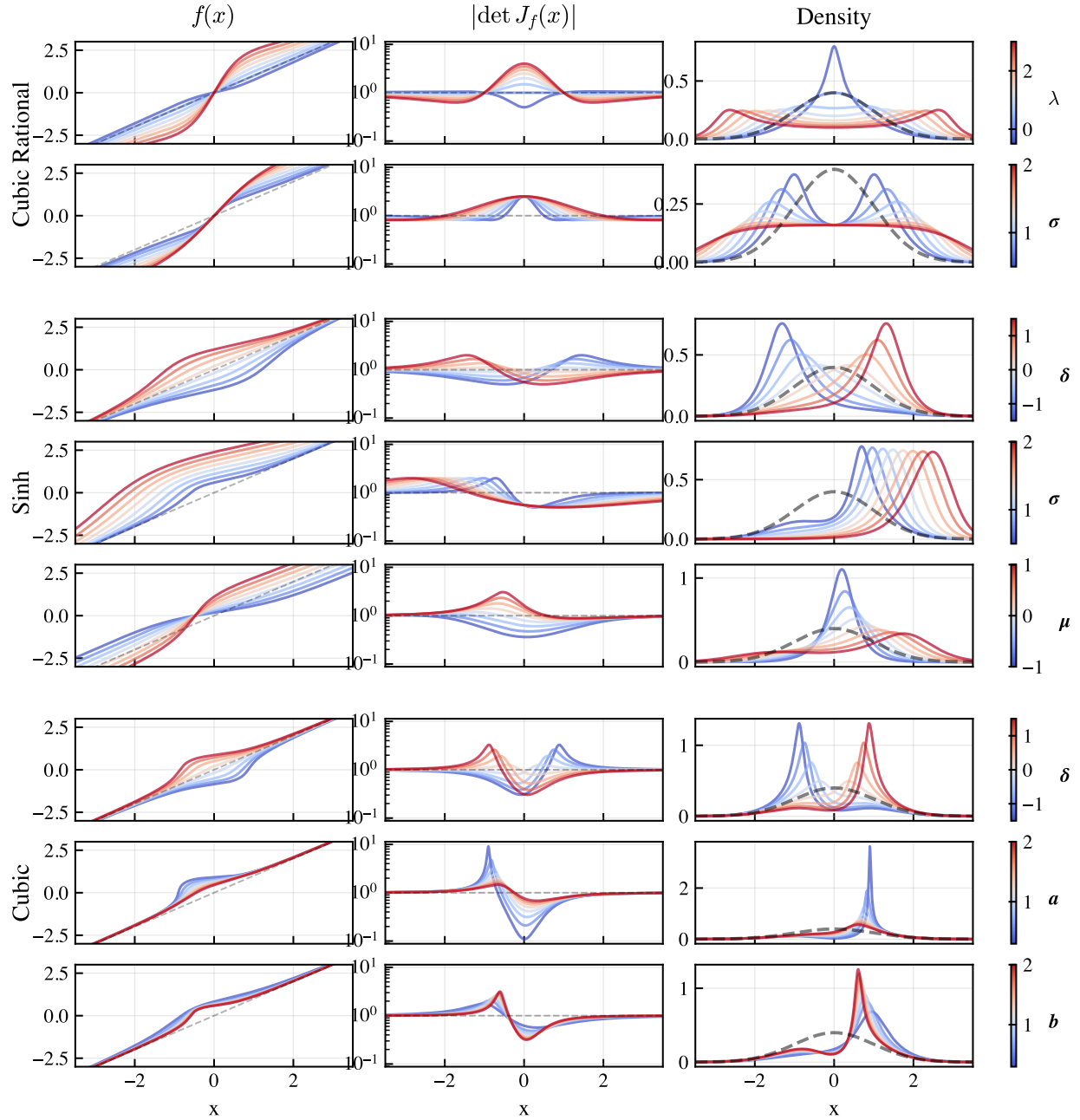


Figure 18: Parameter sweeps for the three analytic bijection types. Each row varies one parameter while holding others fixed. Left column: bijection function $f(x)$ (dashed line shows identity). Middle column: absolute Jacobian determinant $|\det J_f(x)|$ on log scale (dashed line shows 1). Right column: resulting density when applied to a standard normal prior (dashed line shows prior). Color indicates parameter value from low (blue) to high (red).